ORIGINAL PAPER

A three dimensional immersed smoothed finite element method (3D IS-FEM) for fluid–structure interaction problems

Zhi-Qian Zhang · G. R. Liu · Boo Cheong Khoo

Abstract A three-dimensional immersed smoothed finite element method (3D IS-FEM) using four-node tetrahedral element is proposed to solve 3D fluid–structure interaction (FSI) problems. The 3D IS-FEM is able to determine accurately the physical deformation of the nonlinear solids placed within the incompressible viscous fluid governed by Navier-Stokes equations. The method employs the semi-implicit characteristic-based split scheme to solve the fluid flows and smoothed finite element methods to calculate the transient dynamics responses of the nonlinear solids based on explicit time integration. To impose the FSI conditions, a novel, effective and sufficiently general technique via simple linear interpolation is presented based on Lagrangian fictitious fluid meshes coinciding with the moving and deforming solid meshes. In the comparisons to the referenced works including experiments, it is clear that the proposed 3D IS-FEM ensures stability of the scheme with the second order spatial convergence property; and the IS-FEM is fairly independent of a wide range of mesh size ratio.

Keywords Fluid–structure interaction · Finite element method · Immersed boundary · Immersed smoothed finite element method · Characteristic-based split · Incompressible viscous fluid

Z.-Q. Zhang (✉) · B. C. Khoo
Singapore-MIT Alliance (SMA), National University
of Singapore, Singapore 117576, Singapore
e-mail: zhangzhiqian@meshfree.org

G. R. Liu
School of Aerospace Systems, University of Cincinnati,
Cincinnati, OH 45221-0070, USA

B. C. Khoo
Department of Mechanical Engineering, National University
of Singapore, Singapore 119260, Singapore

1 Introduction

Fluid–structure interaction (FSI) with moving boundaries and largely deformable nonlinear solids and structures are challenging problems in numerical simulations in terms of accuracy, robustness and efficiency. With the continual improvements in computer hardware, great efforts have been made by the numerical scientists in the community of computational solid mechanics and fluid dynamics to develop increasingly robust and accurate numerical methodology/technique for the FSI simulation. Among numerous numerical methods for FSI problems, one typical class of methods have been proposed based on the moving-mesh techniques, such as Arbitrary Lagrangian-Eulerian (ALE) methods [1–4], space–time (ST) methods [5–12] and so on. Based on the moving-mesh techniques, the fluid-structure interfaces are explicitly depicted in the discrete model of the FSI system, and the meshes for the fluid and solid structures are movable in the FSI simulations with the moving boundaries or interfaces. Alternatively, based on the immersed-type methods a class of methods using fixed fluid grid or mesh have been proposed, such as the immersed boundary (IB) methods [13–18], immersed finite element method (IFEM) [19–23], 2D immersed smoothed finite element methods (2D IS-FEM) [24,25] and so on. These effective numerical methods to solve FSI problems broadly include three key modules: (1) implementation of the FSIs; (2) solver for transient responses of the nonlinear solids; (3) solver for transient fluid flows.

The first module is always embedded in the process of solving the fluid and solid problems so as to implement the FSIs correctly. The numerical methods for the fluid and solid problems may need meshes or grids to discretize the fluid and solid domains. In the methods based on the moving-mesh techniques, the fluid-structure interface always

Fig. 1 Conceptual illustrations of two types of methods for solving FSI problems: **a** the fluid-structure interfaces always coinciding with fluid mesh or grid; **b** the fluid-structure interfaces immersed inside the fluid mesh or grid
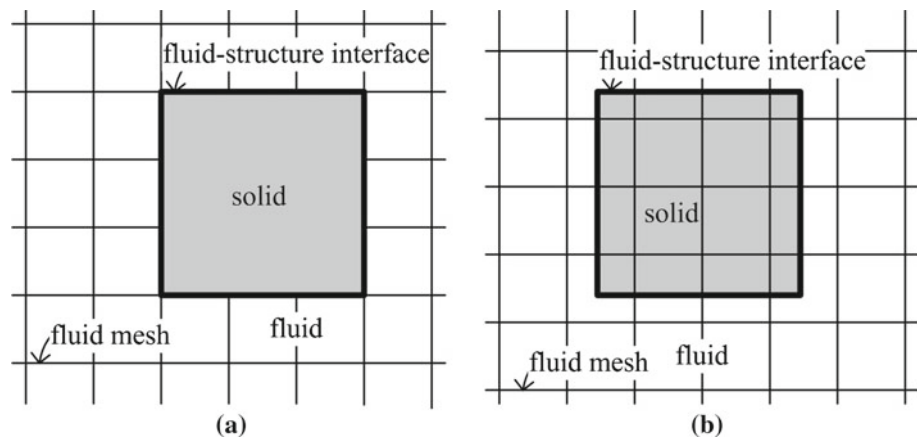
coincide with the fluid mesh or grid, such as the adaptive meshing technique, ALE methods or ST methods, as illustrated in Fig. 1a. In this class of methods the FSIs can be directly imposed on the interface by either the monolithic approach (i.e., the fluid and solid problems are solved simultaneously using a single solver) or the partitioned approach (i.e., the fluid and solid problems are solved separately using two distinct solvers). However, dealing with the problems with moving boundaries, the re-meshing operation is often necessary which is difficult and computational expensive especially for 3D FSI problems. In order to avoid re-meshing, a class of immersed-type methods using fixed fluid grid or mesh has been proposed following the original IB method [13,14], such as the hybrid Cartesian/immersed boundary (HCIB) methods [15–18], IFEM [19–23], 2D IS-FEM [24,25] and so on. The immersed-type methods allow the fluid-structure interface to cut cross the fluid mesh or grid, as shown in Fig. 1b. In most of the IB methods, the fluid domain is discretized by fixed Eulerian mesh or grid, whereas a set of Lagrangian fiber network is used to present the structure being immersed inside the fluid [15–18]. As such, the interactions between the fluid and solid should be carefully treated. A smoothed approximation of the Dirac delta function is designed to distribute the nodal FSI forces and velocity fields between the Eulerian and Lagrangian domains. In 2D problems, the major disadvantage of the IB methods results from the assumption of the one-dimensional fiber-like immersed structure, by which the structure only carries mass but does not occupy volume. Therefore, it is difficult to use IB methods to represent the solids with the complex nonlinear constitutive law, which occupy finite volume in the fluid. To overcome this drawback, IFEM [19–23] has been developed and is able to represent the true physics of the nonlinear solids with the use of the standard FEM procedure. IFEM immerses the whole solid body inside the fluid and imposes the FSI conditions by means of meshfree approximation or FEM interpolation.

Being inspired by the IB and IFEM methods and with the goal of solving general 3D FSI problems, a novel three-dimensional immersed smoothed finite element method (3D IS-FEM) is proposed in this work, which follows the main frame and procedure of the 2D IS-FEM in [25]. This approach adopts the efficient direct forcing technique from IB/HCIB to calculate the FSI force, thus enabling the IS-FEM to analyze the physical motion and deformation of the nonlinear solid as per IFEM. The solvers for the solid and fluid problems in the IS-FEM employ the well-developed numerical methods, such as the smoothed finite element methods (S-FEMs) for the solid part, and the semi-implicit characteristic-based split (CBS) method for the fluid part.

FEM is a popular choice for solving the transient responses of solids and structures. For simple preprocessing, three-node triangular (T3) element for 2D cases and four-node tetrahedral (T4) element for 3D cases are preferred for meshing the domain with complex geometry. However, due to several undesired features such as the overly-stiff behavior, poor accuracy, and difficulties in handling incompressibility, T3 and T4 element are usually not adopted in the standard commercial FEM procedure for solids in which robustness is key. Based on the gradient/strain smoothing technique [26] and the generalized smoothed Galerkin (GS-Galerkin) weak form or weakened weak (W2) form [27–33], a family of S-FEM [34,35] has been proposed, which can greatly improve the performance of the T3 and T4 elements. The 3D IS-FEM mainly utilizes two types of S-FEMs: face-based S-FEM using T4 element (FS-FEM-T4) for compressible solids, and selective S-FEM using T4 element (Selective S-FEM-T4) for nearly incompressible solids. Moreover, as a special case of S-FEM [35], FEM-T4 is adopted in some numerical examples, which serves to demonstrate that our proposed scheme is also available for the standard FEM procedure.

For solving the fluid flow in the FSI problems, any stable and robust numerical method, which is able to use T3 or T4 element and effectively suppress spurious oscillations resulting from the convective characteristic of convection-dominated flows, the restriction of LBB condition and so on, can serve as a suitable candidate for the fluid solver in

IS-FEM. Various reliable numerical methods have been reported to solve the incompressible Navier-Stokes fluid flow under the framework of Galerkin procedure, such as the pressure-stabilizing method introduced in [36] for the Stokes flow and the pressure-stabilizing Pertrov-Galerkin (PSPG) formulation introduced in [37] for Navier-Stokes equations, streamline upwinding/Petrov-Galerkin (SUPG) formulation [38], Galerkin least-square techniques (GLS) [39], Taylor–Galerkin method [40], CBS algorithm [41,42] and so on. In this work, the semi-implicit CBS scheme is employed, which avoids any possibility of spurious solutions. Moreover, one important feature of CBS scheme is that it allows equal interpolation for all the primitive variables, such as the fluid velocity and pressure. Users can employ the simplest four-node triangular (T4) elements for the efficient preprocessing and numerical calculations.

In Sect. 2, the explicit scheme for dynamics analysis of nonlinear solids based on central difference time integration combined with the S-FEM is described. Galerkin procedure based on the semi-implicit CBS method for the incompressible viscous fluid flow is reviewed in Sect. 3. In Sect. 4, the immersed methodology for coupling of the solid and fluid by means of the fictitious Lagrangian fluid mesh is proposed. Following various numerical examples provided in Sect. 5, the conclusions are drawn in Sect. 6.

2 Brief review of S-FEM for explicit dynamics analysis of solids

In order to describe the motion and deformation of the nonlinear solid, assume at the time t (τ) the solid body occupies the solid domain $^\tau\Omega^s$ with a closed boundary $^\tau\Gamma^s$. Here, s denotes the solid appearing as the superscript on the right, while τ denotes the time step number appearing as the superscript on the left. At the initial stage ($\tau = 0$) the solid occupies the domain $^0\Omega^s$ (so called the initial or referential configuration) with the boundary $^0\Gamma^s$. The material coordinates of the solid are denoted as $X_i^s = {}^0x_i^s$, ($i = 1, 2, 3$ for 3-D) at the initial configuration, and at the current configuration of the time t (τ) the spatial coordinates are denoted as $^\tau x_i^s$. The governing equation can be written as the following total Lagrangian description

$$\frac{\partial P_{ji}^s}{\partial X_j^s} + \rho^s g_i = \rho^s a_i^s$$

$$N.B.C. : n_j^s \sigma_{ji}^s = f_i^{t,s} \quad \text{on } \Gamma_t^s;$$
$$V.B.C. : v_i^s = \bar{v}_i^s, \quad \text{on } \Gamma_v^s;$$
$$I.C. : {}^0P_{ji}^s = {}^0\bar{P}_{ji}^s, \quad {}^0v_i^s = {}^0\bar{v}_i^s. \tag{1}$$

Here, N.B.C. denotes the natural boundary conditions, V.B.C. denotes the velocity boundary conditions, and I.C. denotes the initial conditions. In Eq. (1), P_{ji}^s is the first

Piola-Kirchhoff stress tensor, ρ^s is the initial density of the solid, u_i^s is the displacement, a_i^s is the acceleration, v_i^s is the velocity, Γ_t^s is the natural boundary with the outward surface normal n_j^s and the prescribed traction force $f_i^{t,s}$, σ_{ij}^s is the Cauchy stress tensor and Γ_v^s is the essential boundary with the prescribed velocity $\bar{v}_i^s$.

Both S-FEM and the standard FEM (regarded as the special case of S-FEM) are employed in this work. The main difference between S-FEM and FEM is the smoothing operation on the spatial gradient or strain field in S-FEM. Suppose that the initial solid domain $^0\Omega^s$ is discretized by a set of N_n^s nodes and N_{ele}^s elements. The material coordinates of the solid nodes are denoted as X_{Ii}^s ($I = 1$ to N_n^s). In both FEM and S-FEM, the displacement u_i^s and velocity v_i^s are interpolated by the standard FEM procedure:

$$u_i^s = \sum_I {}^0\Phi_I^s u_{Ii}^s, \quad v_i^s = \sum_I {}^0\Phi_I^s v_{Ii}^s, \tag{2}$$

where $^0\Phi_I^s$ is the FEM shape function calculated at the initial configuration. In the standard FEM, the spatial gradient of the field is directly calculated as follows:

$$^0u_{i,j}^s = \sum_I {}^0\Phi_{I,j}^s u_{Ii}^s, \quad ^0v_{i,j}^s = \sum_I {}^0\Phi_{I,j}^s v_{Ii}^s, \tag{3}$$

where $^0\Phi_{I,j}^s = \partial^0\Phi_I^s / X_j^s$ is the derivatives of the shape function at the initial configuration. However, generally the above direct calculations of the spatial gradient are not used in S-FEM, and the smoothing operations on the spatial gradient of the field in the smoothing domains are alternatively required.

In S-FEM, the domain $^0\Omega^s$ is divided into N_{sd}^s non-overlapped smoothing domains $^0\Omega_{isd}^{sd}$ with the boundaries $^0\Gamma_{isd}^{sd}$ ($isd = 1, 2, \ldots, N_{sd}^s$), as illustrated in Fig. 2a. Each smoothing domain $^0\Omega_{isd}^{sd}$ is associated with a representative material point $\mathbf{X}_{isd}^s$. The smoothing of the gradient of the displacement field in $^0\Omega_{isd}^{sd}$ can be implemented as follows:

$$\bar{u}_{i,j}^s \left(\mathbf{X}_{isd}^s\right) = \int\limits_{^0\Omega_{isd}^{sd}} u_{i,j}^s \left(\mathbf{X}^s\right) W\left(\mathbf{X}^s; \mathbf{X}^s - \mathbf{X}_{isd}^s\right) d\Omega \tag{4}$$

where $u_{i,j}^s = \partial u_i^s / \partial X_j^s$ are the gradient of the displacement field, and $\bar{u}_{i,j}^s$ are the so-called *smoothed gradient*. The smoothing function $W\left(\mathbf{X}^s; \mathbf{X}^s - \mathbf{X}_{isd}^s\right)$ should satisfy partition of unity and the following Heaviside type piecewise constant function is employed:

$$W\left(\mathbf{X}^s; \mathbf{X}^s - \mathbf{X}_{isd}^s\right) = \begin{cases} 1/V_{isd}^{sd}, & \mathbf{X}^s \in {}^0\Omega_{isd}^{sd} \\ 0 & \mathbf{X}^s \notin {}^0\Omega_{isd}^{sd} \end{cases};$$
$$V_{isd}^{sd} = volume\left({}^0\Omega_{isd}^{sd}\right). \tag{5}$$

Introducing the divergence theorem, Eq. (5) can be recast to
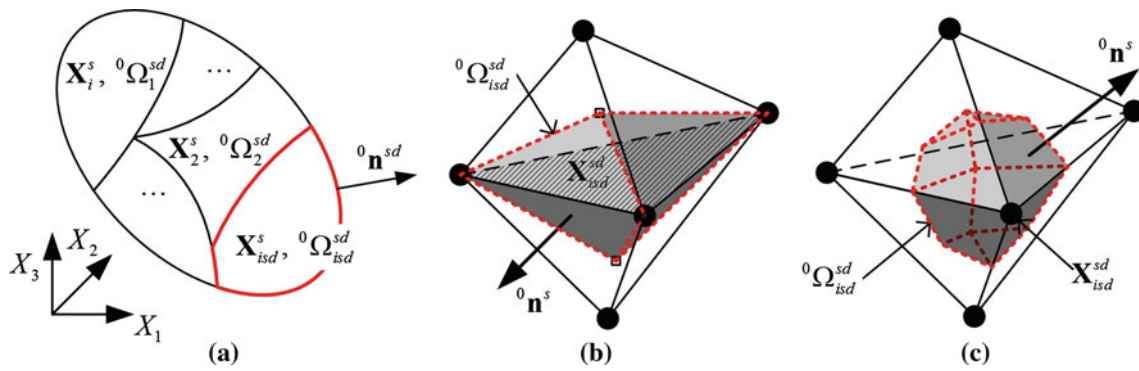
Fig. 2 Illustrations of the smoothing domains for S-FEM: **a** non-overlapping smoothing domain; **b** face-based smoothing domain for FS-FEM-T4; **c** node-based smoothing domain for NS-FEM-T4

$$\bar{u}_{i,j}^s \left(\mathbf{X}_{isd}^s \right) = \frac{1}{V_{isd}^{sd}} \int_{^0\Gamma_{isd}^{sd}} u_i^s \left(\mathbf{X}_{isd}^s \right) {}^0 n_j^{sd} d\Gamma \qquad (6)$$

where ${}^0 n_j^{sd}$ is the outward surface normal of the smoothing domain boundary ${}^0\Gamma_{isd}^{sd}$. Substituting Eq. (2) into Eq. (6), the smoothed gradient of the displacement field can then be written as

$$\bar{u}_{i,j}^s \left(\mathbf{X}_{isd}^s \right) = \sum_I \left(\frac{1}{V_{isd}^{sd}} \int_{^0\Gamma_{isd}^{sd}} {}^0\Phi_I^s \left(\mathbf{X}_{isd}^s \right) {}^0 n_j^{sd} d\Gamma \right) u_{Ii}^s$$

$$= \sum_I {}^0\bar{\Phi}_{I,j}^s \left(\mathbf{X}_{isd}^s \right) u_{Ii}^s \qquad (7)$$

where $\bar{\Phi}_{I,j}^s$ is the *smoothed derivatives of shape function*.

In the finite deformation analysis, the deformation gradient, $F_{ij} = u_{i,j} + \delta_{ij}$, is the primary strain measure. The smoothing operation on the deformation gradient F_{ij} yields the following *smoothed deformation gradient* $\bar{F}_{ij}$:

$$\bar{F}_{ij}^s \left(\mathbf{X}_{isd}^s \right) = \frac{1}{V_{isd}^{sd}} \int_{^0\Gamma_{isd}^{sd}} u_i^s {}^0 n_j^{sd} d\Gamma + \delta_{ij}$$

$$= \sum_I {}^0\bar{\Phi}_{I,j}^s \left(\mathbf{X}_{isd}^s \right) u_{Ii}^s + \delta_{ij}. \qquad (8)$$

Using $\bar{F}_{ij}$, one can easily construct the smoothed Green strain, the smoothed right Cauchy-Green deformation tensor, the smoothed Piola-Kirchhoff stress and so on.

There are mainly two types of smoothing domain in 3D S-FEM with T4 element, such as the face-based smoothing domain as shown in Fig. 2b and the node-based smoothing domain as shown in Fig. 2c, leading to FS-FEM-T4 and node-based smoothed FEM (NS-FEM-T4), respectively. The employment of FS-FEM-T4 can greatly improve the performance of the simplest linear T4 elements and provide superior computational efficiency and accuracy on comparing with the standard FEM-T4 procedure [34,35]. The combination of these two types of S-FEM as Selective S-FEM is used to remove volumetric locking in the analysis of the nearly incompressible solids. The detailed implementations of FS-FEM, NS-FEM and Selective S-FEM can be found in [35].

In this work, the explicit time integration based on the central difference algorithm is employed to obtain the transient dynamics solutions of the nonlinear solids [43]. The well-known equation of motion is given in the following form:

$$M_{IJ}^s a_{Ji}^s = f_{Ii}^{s,ext} - f_{Ii}^{s,int} \qquad (9)$$

subject to the boundary conditions. Here, M_{IJ}^s is the entry of the lumped mass matrix, $f_{Ii}^{s,ext}$ is the external force vector in the standard FEM form, $f_{Ii}^{s,int}$ is the internal force vector, defined in the total Lagrangian formulation as

$$f_{Ii}^{s,int} = \int_{^0\Omega^s} {}^0\Phi_{I,j}^s P_{ji}^s d\Omega. \qquad (10)$$

If FEM is employed, $f_{Ii}^{s,int}$ is calculated following the standard FEM procedure. In S-FEM, $f_{Ii}^{s,int}$ is evaluated based on the smoothed derivatives of the shape function (see [34,35] for details).

In this research, two types of nonlinear elastic materials are employed in the numerical examples. One is the isotropic Saint Venant-Kirchhoff elastic material with the following strain energy density function,

$$\psi \left(\mathbf{E} \right) = \frac{1}{2}\lambda \left(\text{tr}\mathbf{E} \right)^2 + \mu \text{tr}\mathbf{E}^2 \qquad (11)$$

where $\mathbf{E}$ is the Green strain tensor, and λ and μ are the Lamé constants of the linearized theory. The second type is the nearly incompressible Mooney-Rivlin hyperelastic material, defined by the following strain energy density function,

$$\Psi = A_{10} \left(\bar{I}_1 - 3 \right) + A_{01} \left(\bar{I}_2 - 3 \right) + \frac{1}{2}\kappa \left(J - 1 \right) \qquad (12)$$

where A_{10} and A_{01} are the material constants, κ is the bulk modulus, $\bar{I}_1 = I_1 I_3^{-1/3}$ and $\bar{I}_2 = I_1 I_3^{-2/3}$. Here, I_1, I_2 and

I_3 are the three invariants of the right Cauchy-Green deformation tensor $\mathbf{C}$, and J is the determinant of the deformation gradient $\mathbf{F}$. For the nearly incompressible materials some special techniques should be adopted to remove volumetric locking, such as selective reduced integration (SRI) in FEM or Selective S-FEM. If $A_{01} = 0$, the description in Eq. (12) is reduced to Neo-Hookean description.

Using the explicit time integration based on the central difference method [43], we provide the following flowchart to perform the dynamics analysis of the nonlinear solids.

Flowchart 1: Explicit dynamics analysis for nonlinear solids

(1) Loop over all the solid elements, and compute $^0\Phi_I^s$ and $^0\Phi_{I,i}^s$ at the initial configuration.
(2) Compute the lumped mass matrix M_{IJ}^s.
(3) Set up the I.C., $^0v_{Ii}^s$, $^0P_{Iij}^s$, $^0u_{Ii}^s$, and $t(\tau) = 0$ with the time step number $\tau = 0$.
(4) Compute the external force $^{\tau+1}f_I^{s,ext}$.
(5) Call the subroutine **Solid_ExDyna_3D** $(\tau, \Delta t, {}^\tau u_{Ii}^s, {}^\tau v_{Ii}^s, {}^\tau a_{Ii}^s, M_{IJ}^s, {}^{\tau+1}f_{Ii}^{s,ext})$.

  5.1 Compute the (smoothed) internal force $^\tau \bar{f}_{Ii}^{s,int}$, and the residual force $^{\tau+1}f_{Ii}^s = {}^{\tau+1}f_{Ii}^{s,ext} - {}^\tau\bar{f}_{Ii}^{s,int}$.
  5.2 Compute the nodal acceleration $^\tau a_{Ii}^s = M_{IJ}^{-1}{}^{\tau+1}f_{Ii}^s$.
  5.3 Partially update the nodal velocity $^{\tau+1/2}v_{Ii}^s = {}^\tau v_{Ii}^s + \Delta t^\tau a_{Ii}^s/2$.
  5.4 Apply the velocity boundary conditions, and update the nodal displacement $^{\tau+1}u_{Ii}^s = {}^\tau u_{Ii}^s + \Delta t^{\tau+1/2}v_{Ii}^s$.
  5.5 Compute the internal force $^{\tau+1}f_{Ii}^{s,int}$, and the residual force $^{\tau+1}f_{Ii}^s = {}^{\tau+1}f_{Ii}^{s,ext} - {}^{\tau+1}f_{Ii}^{s,int}$.
  5.6 Compute the nodal acceleration $^{\tau+1}a_{Ii}^s = M_{IJ}^{-1}{}^{\tau+1}f_{Ii}^s$.
  5.7 Update the nodal velocity, $^{\tau+1}v_{Ii}^s = {}^{\tau+1/2}v_{Ii}^s + \Delta t^{\tau+1}a_{Ii}^s/2$.
  5.8 Return $^{\tau+1}u_{Ii}^s, {}^{\tau+1}v_{Ii}^s, {}^{\tau+1}a_{Ii}^s$ to the main routine.

(6) Update the solid nodal variables $^\tau u_{Ii}^s = {}^{\tau+1}u_{Ii}^s, {}^\tau v_{Ii}^s = {}^{\tau+1}v_{Ii}^s, {}^\tau a_{Ii}^s = {}^{\tau+1}a_{Ii}^s, \tau = \tau + 1, t = t + \Delta t$. Go to Step (4) and continue with the next time step.

3 Brief review of CBS method for incompressible viscous fluid flow

The conservation form of Navier-Stokes (N-S) equations for the incompressible viscous fluid flow are given as follows

$$\frac{\partial V_i^f}{\partial t} + \frac{\partial}{\partial x_j^f}\left(v_i^f V_j^f\right) = -\frac{\partial p^f}{\partial x_i^f} + \frac{\partial \mathbb{T}_{ij}^f}{\partial x_j^f} + \rho^f g_i$$

$$\frac{\partial V_i^f}{\partial x_i^f} = -\frac{\partial p^f}{\partial t} \; ;$$

$$V.B.C. : \quad g_{vbc}^f(v_i) = v_i^f - \bar{v}_i^f = 0 \quad \text{on } \Gamma_v^f;$$

$$P.B.C. : \quad p^f - \bar{p}^f = 0 \quad \text{on } \Gamma_p^f;$$

$$I.C. : \quad {}^0v_i^f = {}^0\bar{v}_i^f; \quad {}^0p^f = {}^0\bar{p}^f \tag{13}$$

where $V_i^f = \rho^f v_i^f$. Here, P.B.C. denotes the pressure boundary condition. ρ^f is the fluid density, μ^f is the fluid dynamic viscosity, v_i^f is the fluid velocity, p^f is the fluid pressure, g_i is the acceleration of gravity, and $\mathbb{T}_{ij}^f$ is the deviatoric stresses. The superscript f on the right denotes the fluid. The fluid problem is solved based on the Eulerian mesh, hence the nodes of the fluid mesh are fixed with the coordinates x_i^f.

The Galerkin procedure based on the semi-implicit form of CBS method [41,42] is employed to solve the incompressible viscous fluid flow. For the sake of simplicity only the fully-discrete equations are provided here (see [41,42] for the detailed derivations). A set of finite element mesh using T4 elements with N_n^f nodes and N_{ele}^f elements is used to discretize the fluid domain Ω^f. The coordinates of the fluid nodes are denoted by $\mathbf{x}_I^f \left(I = 1 \text{ to } N_n^f\right)$. The primitive unknown variables, the fluid velocity v_i^f and the pressure p^f, can be interpolated by the following standard FEM procedure

$$^\tau v_i^f = \sum_I \Phi_I^f {}^\tau v_{Ii}^f; \quad {}^\tau p^f = \sum_I \Phi_I^f {}^\tau p_I^f \tag{14}$$

where Φ_I^f is the shape function of the fluid node I. Using the above spatial discretization, the time discretization based on the CBS algorithm leads to the following three steps to calculate the fluid velocity and pressure at the new time $t(\tau + 1)$.

Step 1: On the intermediate momentum calculation

$$M_{IJ}^f \frac{{}^*v_{Ji}^f - {}^\tau v_{Ji}^f}{\Delta t} = -{}^\tau C_{IJ}^f {}^\tau v_{Ji}^f - {}^\tau F_{Ii}^f$$
$$- \frac{\Delta t}{2}{}^\tau K_{IJ}^f {}^\tau v_{Ji}^f + {}^\tau f_{Ii}^{f,t} + {}^\tau f_{Ii}^{f,g}$$
$$= {}^*RHS_{Ii}^f + {}^\tau f_{Ii}^{f,g}; \tag{15}$$

Step 2: On the pressure calculation

$$H_{IJ}^f {}^{\tau+1}p_J^f = -\frac{1}{\Delta t}Q_{IJi}^f {}^*v_{Ji}^f; \tag{16}$$

Step 3: On the momentum correction

$$M_{IJ}^f \frac{{}^{\tau+1}v_{Ji}^f - {}^\tau v_{Ji}^f}{\Delta t} = {}^{\tau+1}RHS_{Ii}^f$$
$$= M_{IJ}\frac{{}^*v_{Ji}^f - {}^\tau v_{Ji}^f}{\Delta t} - G_{IJi}^f {}^\tau p_J^f; \tag{17}$$

where,

$$M_{IJ}^f = \int_{\Omega^f} \rho^f \Phi_I^f \Phi_J^f d\Omega,$$

$${}^\tau C_{IJ}^f = \int_{\Omega^f} \rho^f \Phi_I^f \frac{\partial \left({}^\tau v_j^f \Phi_J^f\right)}{\partial x_j^f} d\Omega,$$

$${}^\tau F_{Ii}^f = \int_{\Omega^f} \frac{\partial \Phi_I^f}{\partial x_j^f} {}^\tau \mathbb{T}_{ij}^f d\Omega,$$

$${}^\tau K_{IJ}^f = \int_{\Omega^f} \frac{\partial \left({}^\tau v_k^f \Phi_I^f\right)}{\partial x_k^f} \rho^f \frac{\partial \left({}^\tau v_j^f \Phi_J^f\right)}{\partial x_j^f} d\Omega, \qquad (18)$$

$${}^\tau f_{Ii}^{f,t} = \int_{\Gamma^f} \Phi_I^f {}^\tau \mathbb{T}_{ij}^f n_j^f d\Gamma, \quad {}^\tau f_{Ii}^{f,g} = \int_{\Omega^f} \Phi_I^f \rho^f g_i d\Omega,$$

$$H_{IJ}^f = \int_{\Omega^f} \frac{\partial \Phi_I^f}{\partial x_i^f} \frac{\partial \Phi_J^f}{\partial x_i^f} d\Omega, \quad Q_{IJi}^f = \int_{\Omega^f} \rho^f \Phi_I^f \frac{\partial \Phi_J^f}{\partial x_i^f} d\Omega,$$

$$G_{IJi}^f = \int_{\Omega^f} \Phi_I^f \frac{\partial \Phi_J^f}{\partial x_i^f} d\Omega, .$$

The mass matrix M_{IJ}^f in the above equations is lumped. Under Step 2, the iteration scheme, the preconditioned conjugate gradient (PCG) scheme, is employed to solve Eq. (16). The invariant matrices H_{IJ}^f and M_{IJ}^f are assembled only once at the beginning. The right hand sides under Step 1 and Step 3, denoted by ${}^* RHS_{Ii}^f$ and ${}^{\tau+1} RHS_{Ii}^f$, respectively, will be used in the calculation of the FSI forces. The above semi-implicit CBS algorithm is conditionally stable, and the critical time step Δt can be determined accordingly [42,44]. The flowchart to calculate the incompressible viscous fluid flow is given below.

Flowchart 2: CBS for incompressible viscous fluid

(1) Loop over all the fluid elements, and compute Φ_I^f and $\partial \Phi_I^f / \partial x_i^f$.

(2) Compute the lumped mass matrix M_{IJ}^f and the matrix H_{IJ}^f.

(3) Set up I.C., ${}^0 v_{Ii}^f, {}^0 p_{Ii}^f, t(\tau) = 0$, and the time step number $\tau = 0$.

(4) Call subroutine **Fluid_CBS_3D** $(\tau, \Delta t, {}^\tau v_{Ii}^f, {}^\tau p_{Ii}^f, M_{IJ}^f, H_{IJ}^f, {}^{\tau+1} g_{vbc}^f (v_{Ii}^f))$.

    4.1 Compute ${}^* v_{Ji}^f$ using Eq. (15).

    4.2 Apply the P.B.C., and obtain ${}^{\tau+1} p_J^f$ using Eq. (16).

    4.3 Use Eq. (17) and apply V.B.C. ${}^{\tau+1} g_{vbc}^f (v_{Ii})$ to get ${}^{\tau+1} v_{Ji}^f$.

    4.4 Return ${}^{\tau+1} v_{Ji}^f$ and ${}^{\tau+1} p_I^f$ to the main routine.

(5) Update ${}^\tau v_{Ii}^f = {}^{\tau+1} v_{Ii}^f, {}^\tau p_I^f = {}^{\tau+1} p_I^f, \tau = \tau + 1$ and $t = t + \Delta t$. Go to Step (4) and continue with the next time step.

4 Immersed S-FEM for FSI

4.1 Governing equations and FSI conditions

In this work, the 3D FSI problem involves a deformable nonlinear solid body immersed within the incompressible viscous fluid. As illustrated in Fig. 3, firstly we assume that the fluid always exists everywhere in the fluid domain Ω^f. The solid domain ${}^\tau \Omega^s$ is always completely immersed inside Ω^f. The sub-domain of Ω^f overlapping the solid domain ${}^\tau \Omega^s$ is denoted by ${}^\tau \Omega^{fs} = {}^\tau \Omega^s$ with a closed fluid-structure interface ${}^\tau \Gamma^{fs} = {}^\tau \Gamma^s$. Obviously, this FSI problem consists of a fluid and a solid part. These two parts are coupled by additional FSI conditions. The FSI conditions in this research are introduced based on the following assumption: the fluid particles residing in Ω^{fs} are bound to the solid particles, i.e., the motions of the fluid particles in Ω^{fs} are identical to the motions of the bound solid particles. This assumption is presented by the FSI velocity condition in Eq. (19). The mentioned assumption indicates the non-slip condition at the fluid-structure interface. The FSI forcing condition in Eq. (19) reveals that, when the solid and fluid particles in Ω^{fs} are constrained to satisfy the first equation of Eq. (19), a pair of interacting forces, $f_i^{s,FSI}$ and $f_i^{f,FSI}$, appear and are applied on the solid and fluid particles, respectively.

Overall, the governing equations for the FSI problems comprise three parts: (1) the governing equations for the fluid flow given by Eq. (13); (2) the governing equation for the solid given by Eq. (1); (3) the FSI conditions given as follows.

FSI conditions

FSI velocity condition: $v_i^f = v_i^s$ for $\mathbf{x} \in \Omega^{fs}$;

FSI forcing condition: $f_i^{s,FSI} = -f_i^{f,FSI}$ for $\mathbf{x} \in \Omega^{fs}$.

$$(19)$$

The solution scheme for the IS-FEM is composed of three main modules: (1) solving the fluid problem with the FSI conditions; (2) solving the solid problem with the FSI conditions; and (3) identify the FSI conditions. The key point is to identify and implement the FSI conditions in Eq. (19) properly and accurately. In the proposed IS-FEM, the FSI velocity condition is imposed on the fluid particles in ${}^\tau \Omega^{fs}$, and the corresponding FSI forcing condition is applied as the external force acting on the solid particles. The FSI velocity condition can be achieved straightforwardly from the solid velocity field. However, the FSI forces have to be determined carefully. Below shows the detailed algorithm to advance the solutions at the next time step $\tau + 1$ from the time step τ.

In the formulations, the fluid problem is solved in the whole fluid domain including the overlapping domain Ω^{fs},
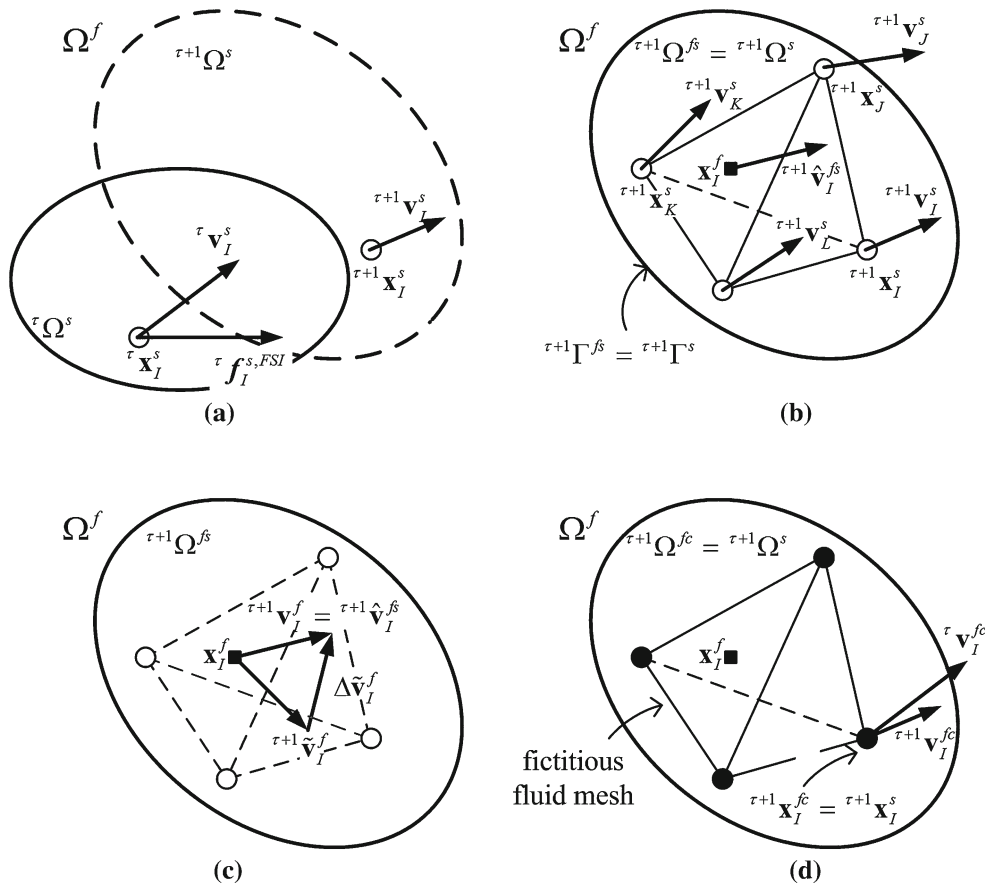
Fig. 3 Procedure for the IS-FEM to solve FSI problems from the time step τ to the time step $\tau+1$: **a** solve the solid problem and update the solid configuration, **b** obtain the velocity of fluid nodes $\mathbf{x}_I^f \in {}^{\tau+1}\Omega^{fs}$ by FEM interpolation, **c** solve the fluid problem with FSI velocity condition, **d** illustration of fictitious fluid mesh and fictitious fluid nodes. *Open circle* solid nodes; *filled square* fluid nodes; *filled circle* fictitious fluid nodes

with the proper B.C., I.C. and FSI conditions. Similarly, under the given I.C., B.C. and the proper FSI conditions, the motion and deformation of the nonlinear solid body are calculated taking into account simultaneously the interactions with the fluid.

The fluid domain Ω^f and the solid domain ${}^{\tau}\Omega^s$ are discretized by two different sets of meshes, respectively. The fluid problem is solved using Eulerian mesh, and the solid problem is solved using Lagrangian mesh. These two sets of meshes are not required to coincide. It is also not necessary to adopt the same type of the element. In this work, only the simplest linear element, four-node tetrahedral (T4) element, is employed for the 3D simulations.

To establish the solution procedure of IS-FEM in the following sub-sections, firstly we assume that, at the time $t\,(\tau)$, the status of the fluid and solid are already known, i.e., ${}^{\tau}v_{Ii}^f$, ${}^{\tau}p_I^f$, ${}^{\tau}v_{Ii}^s$, ${}^{\tau}a_{Ii}^s$, ${}^{\tau}u_{Ii}^s$, and the FSI force ${}^{\tau}f_{Ii}^{s,FSI}$ are known variables. At the initial stage $\tau = 0$, all these variables can be given as the initial conditions. The boundary conditions for the solid and fluid problems expressed in

Eqs. (1) and (13) apart from the fluid–structure interaction, are satisfied by default without special indication in this section.

4.2 Solving the solid problem with FSI forcing condition

We start the FSI analysis by solving for the motion and deformation of the solid in terms of the known nodal values ${}^{\tau}v_{Ii}^s$, ${}^{\tau}a_{Ii}^s$, and ${}^{\tau}u_{Ii}^s$ at the time step τ. The nodal FSI forces ${}^{\tau}f_{Ii}^{s,FSI}$ are computed from the fluid status ${}^{\tau}v_{Ii}^f$ and ${}^{\tau}p_I^f$ at the time step τ (see details in the Subsect. 4.4), and assembled to the total external force as follows

$${}^{\tau+1}\tilde{f}_{Ii}^{s,ext} = {}^{\tau+1}f_{Ii}^{s,ext} + {}^{\tau}f_{Ii}^{s,FSI}. \tag{20}$$

Applying the total external force ${}^{\tau+1}\tilde{f}_{Ii}^{s,ext}$ on the solid nodes, and calling the subroutine *Solid_ExDyna_3D* in the Flowchart 1, one can solve for the solid variables ${}^{n+1}v_{Ii}^s$, ${}^{n+1}a_{Ii}^s$, and ${}^{n+1}u_{Ii}^s$. And the configuration ${}^{\tau}\Omega^s$ of the solid is then transformed to ${}^{\tau+1}\Omega^s$. The overlapping

domain $^\tau\Omega^{fs}$ is transformed to $^{\tau+1}\Omega^{fs} = {}^{\tau+1}\Omega^s$, as plotted in Fig. 3a.

4.3 Identifying FSI velocity condition and solving fluid problem

As the outcome of the Subsect. 4.2, the nodal velocities $^nv^s_{Ii}$ and $^{n+1}v^s_{Ii}$ are known for all the solid nodes. Because the fluid and solid meshes usually do not coincide, the FSI velocity condition $v^f_i = v^s_i$ for $\mathbf{x} \in \Omega^{fs}$ can not be imposed on the fluid nodes $\mathbf{x}^f_I \in {}^{\tau+1}\Omega^{fs}$ directly. Hence, data fitting techniques have to be employed to map the solid velocity field to the fluid nodes. One of the most frequently used tools is the discretized Dirac delta function in IB methods [13,14], and the similar procedure using meshfree approximation [21]. In this work, a simple linear interpolation scheme with the help of the fluid and solid FEM meshes is utilized, which has been reported in [23].

To implement the FEM interpolation, a search algorithm has to be carried out to find which solid element at the configuration $^{\tau+1}\Omega^s$ covers the fluid node $\mathbf{x}^f_I \in {}^{\tau+1}\Omega^{fs}$ of interest. Due to the motion and deformation of the solid body, this searching procedure has to be carried out at every time step after the new configuration $^{\tau+1}\Omega^s$ is obtained. After searching, for every fluid node $\mathbf{x}^f_I \in {}^{\tau+1}\Omega^{fs}$, one can find a corresponding solid element covering it. One should note that one solid element may cover more than one fluid node. Suppose a solid element with the nodes $^{\tau+1}\mathbf{x}^s_I$, $^{\tau+1}\mathbf{x}^s_J$, $^{\tau+1}\mathbf{x}^s_K$, and $^{\tau+1}\mathbf{x}^s_L$ is found to be covering the fluid node $\mathbf{x}^f_I \in {}^{n+1}\Omega^{fs}$ of interest, as shown in Fig. 3b. The solid velocity field can be interpolated to this fluid node so as to obtain the velocity $^{\tau+1}\hat{v}^{fs}_{Ii}$ as follows

$$^{\tau+1}\hat{v}^{fs}_{Ii} = \sum_{a=I,J,K,L} {}^{\tau+1}\Phi^s_a\left(^{\tau+1}\mathbf{x}^f_I\right){}^{\tau+1}v^s_{ai} \tag{21}$$

$$\left(\text{for } \mathbf{x}^f_I \in {}^{\tau+1}\Omega^{fs}\right)$$

where $^{\tau+1}\Phi^s_a\left(^{\tau+1}\mathbf{x}^f_I\right)$ is the FEM shape function at the configuration $^{\tau+1}\Omega^s$. The FSI velocity condition can then be identified, and imposed on the fluid nodes $\mathbf{x}^f_I \in {}^{n+1}\Omega^{fs}$ in the following form

$$^{\tau+1}g^f_{FSI}\left(v^f_{Ii}\right) = {}^{\tau+1}v^f_{Ii}$$
$$- {}^{\tau+1}\hat{v}^{fs}_{Ii} = 0, \quad \mathbf{x}^f_I \in {}^{\tau+1}\Omega^{fs}. \tag{22}$$

Appending $^{n+1}g^f_{FSI}\left(v^f_{Ii}\right)$ to $^{n+1}g^f_{vbc}\left(v^f_{Ii}\right)$ leads to the following modified fluid V.B.C:

$$^{\tau+1}g^f_{vbc\cup FSI}\left(v^f_{Ii}\right): \ {}^{\tau+1}v^f_{Ii} = {}^{\tau+1}\bar{v}^f_{Ii},$$

$$\mathbf{x}^f_I \in \Gamma^f_v \text{ and}$$
$$^{\tau+1}v^f_{Ji} = {}^{\tau+1}\hat{v}^{fs}_{Ji}, \quad ^{\tau+1}\mathbf{x}^f_J \in {}^{\tau+1}\Omega^{fs}. \tag{23}$$

Simply replacing $^{\tau+1}g^f_{vbc}\left(v^f_{Ii}\right)$ by $^{\tau+1}g^f_{vbc\cup FSI}\left(v^f_{Ii}\right)$ in the call on the subroutine *Fluid_CBS_3D* in the Flowchart 2, the fluid status will be updated. The results of this step are the fluid velocity $^{\tau+1}v^f_{Ii}$ which satisfies the fluid V.B.C. and the FSI velocity condition, and the fluid pressure $^{n+1}p^f_I$ which satisfies the fluid P.B.C.

4.4 Identifying FSI forcing condition

The scheme to calculate the FSI forces acting on the fluid and solid particles is similar to the direct forcing method [15] or the first-order temporal differencing method [16]. As described in Sect. 4.2, the FSI velocity condition is directly imposed on the fluid nodes. However, if the Navier-Stokes equations are solved without the FSI velocity condition $^{\tau+1}g^f_{FSI}\left(v^f_{Ii}\right)$, i.e., the fluid particles $\mathbf{x}^f \in {}^{\tau+1}\Omega^{fs}$ are not bound to the corresponding solid particles, the CBS procedure will lead to the nodal fluid velocities $^{\tau+1}\tilde{v}^f_{Ii}$, which can be written in the following form in terms of Eq. (17)

$$M^f_{IJ}\frac{^{\tau+1}\tilde{v}^f_{Ji} - {}^\tau v^f_{Ji}}{\Delta t} = {}^{\tau+1}RHS^f_{Ii}. \tag{24}$$

In the Subsect. 4.3, the nodal fluid velocities solved satisfying the FSI velocity condition are $^{\tau+1}v^f_{Ii}$. On the fluid nodes $\mathbf{x}^f_I \in {}^{\tau+1}\Omega^{fs}$, one may note that $^{\tau+1}\tilde{v}^f_{Ii}$ are different from the $^{\tau+1}v^f_{Ii}$. Suppose the nodal force $^{\tau+1}f^{f,FSI}_{Ii}$ is applied on each of the fluid nodes $\mathbf{x}^f_I \in {}^{\tau+1}\Omega^{fs}$ so as to introduce a velocity increment Δv^f_{Ji}, thereby enabling the $^{\tau+1}\tilde{v}^f_{Ji}$ to take on $^{\tau+1}v^f_{Ii}$,(as illustrated in Fig. 3c), we have

$$^{\tau+1}v^f_{Ii} = {}^{\tau+1}\tilde{v}^f_{Ii} + \Delta v^f_{Ii} \quad \left(\mathbf{x}^f_I \in {}^{\tau+1}\Omega^{fs}\right). \tag{25}$$

Furthermore, the change of $^\tau v^f_{Ii}$ to $^{\tau+1}v^f_{Ii}$ can be viewed as the result of the nodal forces $^{\tau+1}F^f_{Ii}$ acting on the fluid nodes $\mathbf{x}^f_I \in {}^{\tau+1}\Omega^{fs}$ through the period from $t(\tau)$ to $t(\tau+1)$, as provided in the following form

$$M^f_{IJ}\frac{^{\tau+1}v^f_{Ji} - {}^\tau v^f_{Ji}}{\Delta t} = {}^{\tau+1}F^f_{Ii} \quad \left(\text{for } \mathbf{x}^f_I \in {}^{\tau+1}\Omega^{fs}\right). \tag{26}$$

Substitution of Eqs. (24) and (25) into Eq. (26) yields

$$M^f_{IJ}\frac{^{\tau+1}v^f_{Ji} - {}^\tau v^f_{Ji}}{\Delta t} = M^f_{IJ}\frac{\left(^{\tau+1}\tilde{v}^f_{Ji} + \Delta v^f_{Ji}\right) - {}^\tau v^f_{Ji}}{\Delta t}$$
$$= {}^{\tau+1}RHS^f_{Ii} + {}^{\tau+1}f^{f,FSI}_{Ii} \quad \left(\text{for } \mathbf{x}^f_I \in {}^{\tau+1}\Omega^{fs}\right). \tag{27}$$

Next, one can recast the above equation considering Eqs. (15) and (17) as

$$
\begin{aligned}
^{\tau+1}f^{f,FSI}_{Ii} &= M^f_{IJ}\frac{^{\tau+1}v^f_{Ji}-{}^\tau v^f_{Ji}}{\Delta t}-{}^{\tau+1}RHS^f_{Ii}\\
&= M^f_{IJ}\frac{^{\tau+1}v^f_{Ji}-{}^\tau v^f_{Ji}}{\Delta t}-{}^*RHS^f_{Ii}\\
&\quad + G^f_{IJi}{}^{\tau+1}p^f_J.
\end{aligned}
\tag{28}
$$

According to the FSI forcing condition, the FSI forces as applied on the solid can be obtained by $^{\tau+1}f^{s,FSI}_i = -{}^{\tau+1}f^{f,FSI}_i$. However, because the solid mesh usually does not coincide with the fluid mesh, the FSI force $^{\tau+1}f^{s,FSI}_i$ can not be directly achieved by the integrations in Eq. (18) on the fluid mesh.

Note the assumption that the fluid particles are bound to the solid particles, so that each solid node $^{\tau+1}\mathbf{x}^s_I$ carries one fictitious fluid node $^{\tau+1}\mathbf{x}^{fc}_I = {}^{\tau+1}\mathbf{x}^s_I$. Naturally, these fictitious fluid nodes can be used to construct a mesh coinciding with the solid mesh, so called the fictitious fluid mesh. The fictitious nodes and fictitious fluid mesh defined on the fictitious fluid domain $^{\tau+1}\Omega^{fc}$ are illustrated in Fig. 3d. All these fictitious fluid particles possess the fluid properties, velocity and pressure. Due to the FSI velocity condition, the nodal velocities $^{\tau+1}v^{fc}_{Ii}$ of these fictitious fluid nodes $^{\tau+1}\mathbf{x}^{fc}_I$ can be immediately obtained via

$$
^\tau v^{fc}_{Ii} = {}^\tau v^s_{Ii}; \quad ^{\tau+1}v^{fc}_{Ii} = {}^{\tau+1}v^s_{Ii} \quad \left(^{\tau+1}\mathbf{x}^{fc}_I = {}^{\tau+1}\mathbf{x}^s_I\right)
\tag{29}
$$

A search process is invoked to find the fluid element covering the fictitious fluid node $^{\tau+1}\mathbf{x}^{fc}_I$ of interest for obtaining the value of the fluid pressure field on these fictitious fluid nodes. Suppose the fluid element with the nodes $^{\tau+1}\mathbf{x}^f_I$, $^{\tau+1}\mathbf{x}^f_J$, $^{\tau+1}\mathbf{x}^f_K$, and $^{\tau+1}\mathbf{x}^f_L$ is found which covers the fictitious fluid node $^{\tau+1}\mathbf{x}^{fc}_I$ of interest, one can perform the following interpolation to calculate the pressure value on the fictitious fluid node $\mathbf{x}^{fc}_I$

$$
^\tau p^{fc}_I = \sum_{a=I,J,K,L} \Phi^f_a\left(^{\tau+1}\mathbf{x}^{fc}_I\right){}^\tau p^f_a
\tag{30}
$$

where $\Phi^f_a\left(^{\tau+1}\mathbf{x}^{fc}_I\right)$ is the shape function of the fluid element. It is worth noting that, the fictitious fluid mesh is not featured in the calculations for the fluid part as outlined in the Subsect. 4.5, and is only used to perform the FEM interpolation and to evaluate the following numerical integration.

The FSI force $^{\tau+1}f^{s,FSI}_{Ii}$ can be evaluated on the fictitious fluid mesh, as follows

$$
\begin{aligned}
^{\tau+1}f^{s,FSI}_{Ii} &= -{}^{\tau+1}f^{fc,FSI}_{Ii}\\
&= -M^{fc}_{IJ}\frac{^{\tau+1}v^{fc}_{Ji}-{}^\tau v^{fc}_{Ji}}{\Delta t}\\
&\quad -{}^\tau C^{fc}_{IJ}{}^\tau v^{fc}_{Ji}-{}^\tau F^{fc}_{Ii}-\frac{\Delta t}{2}{}^\tau K^{fc}_{IJ}{}^\tau v^{fc}_{Ji}+G^{fc}_{IJi}{}^\tau p^{fc}_J\\
&= -M^{fc}_{IJ}\frac{^{\tau+1}v^{fc}_{Ji}-{}^\tau v^{fc}_{Ji}}{\Delta t}
\end{aligned}
$$

$$
-\int_{^{\tau+1}\Omega^{fc}} \rho^f\Phi^{fc}_I\frac{\partial\left(^\tau v^{fc}_j\Phi^{fc}_J\right)}{\partial x^{fc}_j}{}^\tau v^{fc}_{Ji}d\Omega
$$

$$
-\int_{^{\tau+1}\Omega^{fc}} \frac{\partial\Phi^{fc}_I}{\partial x^{fc}_j}{}^\tau\mathbb{T}^{fc}_{ij}d\Omega
$$

$$
-\frac{\Delta t}{2}\int_{^{\tau+1}\Omega^{fc}} \rho^f\frac{\partial\left(^\tau v^{fc}_k\Phi^{fc}_I\right)}{\partial x^{fc}_k}\frac{\partial\left(^\tau v^{fc}_j\Phi^{fc}_J\right)}{\partial x^{fc}_j}{}^\tau v^{fc}_{Ji}d\Omega
$$

$$
+\int_{^{\tau+1}\Omega^{fc}} \Phi^{fc}_I\frac{\partial\Phi^{fc}_J}{\partial x^{fc}_i}{}^\tau p^{fc}_J d\Omega.
\tag{31}
$$

The gradient of the velocity $\partial^\tau v^{fc}_i/\partial x^{fc}_j$ and the spatial derivatives of the shape function $\partial^\tau\Phi^{fc}_I/\partial x^{fc}_i$ need to be updated at the current configuration $^{\tau+1}\Omega^{fc}$, and the integrations are computed numerically using the fictitious fluid mesh.

Strictly, the components of the FSI force in Eq. (31) are equivalent to the drag and lift forces applied on the solid immersed in the fluid. Neglecting the second order term of Δt on the right hand side of Eq. (31), one can recast Eq. (31) in terms of the divergence theorem

$$
\begin{aligned}
f^{s,FSI}_{Ii} &= -\int_\Omega \rho\Phi_I\frac{\Delta v_i}{\Delta t}d\Omega - \int_\Omega \rho\Phi_I\frac{\partial\left(v_j v_i\right)}{\partial x_j}d\Omega\\
&\quad -\int_\Omega \frac{\partial\Phi_I}{\partial x_j}\mathbb{T}_{ij}d\Omega + \int_\Omega \Phi_I\frac{\partial p}{\partial x_i}d\Omega\\
&= -\int_\Omega \rho\Phi_I\frac{\Delta v_i}{\Delta t}d\Omega - \int_\Gamma \rho\Phi_I v_i n_i d\Omega\\
&\quad -\int_\Gamma \Phi_I\mathbb{T}_{ij}n_j d\Omega + \int_\Gamma \Phi_I p n_i d\Omega.
\end{aligned}
\tag{32}
$$

The summing up of the nodal forces $f^{s,FSI}_{Ii}$ yields the following which are the same as the drag and lift forces found in [45] often used in CFD,

$$
\begin{aligned}
f^{s,FSI}_i &= \sum_I f^{s,FSI}_{Ii} = -\int_\Omega \rho\frac{\Delta v_i}{\Delta t}d\Omega - \int_\Gamma \rho v_i n_i d\Omega\\
&\quad -\int_\Gamma \mathbb{T}_{ij}n_j d\Omega + \int_\Gamma p n_i d\Omega.
\end{aligned}
\tag{33}
$$

4.5 Solution procedure for IS-FEM

Following the detailed discussions in the above subsections, the overall procedure for 3D IS-FEM is presented below.

Flowchart 3: 3D IS-FEM for FSI problems

(1) Initialization: Discretize the fluid domain Ω^f and solid domain ${}^0\Omega^s$ at initial configuration; compute ${}^0\Phi^s_I$, ${}^0\bar{\Phi}^s_{I,i}$, Φ^f_I, $\Phi^f_{I,i}$, the lumped the mass matrices M^s_{IJ}, M^f_{IJ}, $M^{fc}_{IJ} = M^s_{IJ}$ and the matrix H^f_{IJ}.

(2) Set up the I.C.: for fluid, ${}^0v^f_{Ii}$ and ${}^0p^f_{Ii}$; for solid, ${}^0v^s_{Ii}$ and ${}^0P^s_{Iij}$; and the initial FSI force ${}^0f^{s,FSI}_{Ii}$.

(3) Set the time step counter $\tau = 0$ and $t(\tau) = 0$.

(4) Calculate ${}^{\tau+1}\tilde{f}^{s,ext}_{Ii} = {}^{\tau+1}f^{s,ext}_{Ii} + {}^{\tau}f^{s,FSI}_{Ii}$.

(5) Call the subroutine *Solid_ExDyna_3D* (τ, Δt, ${}^{\tau}u^s_{Ii}$, ${}^{\tau}v^s_{Ii}$, ${}^{\tau}a^s_{Ii}$, M^s_{IJ}, ${}^{\tau+1}\tilde{f}^{s,ext}_{Ii}$) and obtain ${}^{\tau+1}u^s_{Ii}$, ${}^{\tau+1}v^s_{Ii}$, and ${}^{\tau+1}a^s_{Ii}$. Update the coordinates of solid nodes as ${}^{\tau+1}x^s_{Ii} = {}^{\tau}x^s_{Ii} + {}^{\tau+1}u^s_{Ii}$.

(6) Calculate ${}^{\tau+1}\hat{v}^f_{Ii}$ for $\mathbf{x}^f_I \in {}^{\tau+1}\Omega^{fs}$ via the FEM interpolation in Eq. (21).

(7) Construct the new modified fluid V.B.C. ${}^{\tau+1}g^f_{vbc\cup FSI}\left(v^f_{Ii}\right)$ in Eq. (23).

(8) Call the subroutine *Fluid_CBS_3D*(τ, Δt, ${}^{\tau}v^f_{Ii}$, ${}^{\tau}p^f_{Ii}$, M^f_{IJ}, H^f_{IJ}, ${}^{\tau+1}g^f_{vbc\cup FSI}\left(v^f_{Ii}\right)$) and obtain ${}^{\tau+1}v^f_{Ii}$ and ${}^{\tau+1}p^f_I$.

(9) Call the subroutine *FSI_Force_3D* (${}^{\tau+1}x^s_{Ii}$, ${}^{\tau+1}v^s_{Ii}$, ${}^{\tau+1}p^{fc}_I$).

  9.1 Update the coordinates of fictitious fluid node ${}^{\tau+1}x^{fc}_{Ii} = {}^{\tau+1}x^s_{Ii}$;

  9.2 Calculate ${}^{\tau+1}\Phi^{fc}_{I,i}$.

  9.3 Get the nodal fluid velocities at fictitious fluid nodes ${}^{\tau+1}v^{fc}_{Ii} = {}^{\tau+1}v^s_{Ii}$, ${}^{\tau}v^{fc}_{Ii} = {}^{\tau}v^s_{Ii}$.

  9.4 Calculate ${}^{\tau+1}p^{fc}_I$ via the FEM interpolation in Eq. (30).

  9.5 Calculate ${}^{\tau+1}f^{s,FSI}_{Ii}$ using Eq. (31), and return to the main routine.

(10) Update the variables: ${}^{\tau}v^f_{Ii} = {}^{\tau+1}v^f_{Ii}$, ${}^{\tau}p^f_I = {}^{\tau+1}p^f_I$, ${}^{\tau}u^s_{Ii} = {}^{\tau+1}u^s_{Ii}$, ${}^{\tau}v^s_{Ii} = {}^{\tau+1}v^s_{Ii}$, ${}^{\tau}a^s_{Ii} = {}^{\tau+1}a^s_{Ii}$, ${}^{\tau}f^{f,FSI}_{Ii} = {}^{\tau+1}f^{f,FSI}_{Ii}$, ${}^{\tau}x^s_{Ii} = {}^{\tau+1}x^s_{Ii}$, $\tau = \tau + 1$, $t(\tau) = t(\tau) + \Delta t$; go to Step. (6) and continue with the next time step.

In the solution procedure, both the CBS for the fluid part and the explicit time integration for the solid part are conditionally stable, so the time step Δt has to be chosen carefully. The critical time step Δt_{cr} is determined by $\Delta t_{cr} = \min\left(\Delta t^s_{cr}, \Delta t^f_{cr}\right)$. The Δt^s_{cr} is the critical time step for the solid problem, determined by the size of solid elements and material properties (see details in [43]). The CBS method in [41,42] provides the means to determine the critical time step Δt^f_{cr}. In this research, the constant time step is used which satisfies $\Delta t < \Delta t_{cr}$.

Previous works on finite element immersed boundary method have reported that the ratio h^f/h^s between the Eulerian fluid mesh size h^f and Lagrangian solid mesh size h^s can affect the stability of IB method [22,46]. There is also a suggestion that the size of the fluid mesh should not be too small compared to the solid mesh in order to prevent any unphysical "leaking" phenomenon [20,23] in IFEM. In the proposed 2D IS-FEM [25], the effect of the ratio h^f/h^s is investigated numerically, which clearly demonstrates no numerical artifact is observed even for very fine fluid mesh used, and the stability fairly independent of a wide range of the mesh size ratio is assured. In the 3D IS-FEM, the numerical examples in Sect. 5 also demonstrate the stability of the 3D IS-FEM is not affected by the ratio h^f/h^s for a wide range similar to the 2D IS-FEM. In the 3D IS-FEM, there is no strict limitation to h^f/h^s, which is usually selected to be 0.25–2.0.

Another common numerical issue is the incompressibility constraint of the solid. Some numerical methods require computational expensive volume correction algorithms [23]. For the IS-FEM using volumetric-locking-free Selective S-FEM, there is no additional volume correction operation required to satisfy the incompressibility constraint, because it is able to solve the physical deformation of the nearly-incompressible solids in terms of the constitutive law. If the solid material is compressible, the IS-FEM using FS-FEM for 3D or ES-FEM for 2D also works for the cases with small strains or small volume changes such as beam bending problem.

5 Numerical examples

5.1 Piston in a tunnel with incompressible viscous fluid (Example 5.1)

A solid piston moving inside a tunnel with a square cross-section is analyzed in this example, as illustrated in Fig. 4. The geometry parameters of the fluid and solid domains are given by $a = 0.5$ m, $b = 2$ m, $d = 0.5$ m. At the initial position of the piston, $l = 0.1$ m. The properties of the incompressible viscous fluid are $\rho^f = 1.0$ kg/m^3 and $\mu^f = 0.1$ Pa s. The solid piston is modeled as St. Venant material with the following properties: the density $\rho^s = 1.0 \times 10^3$ kg/m^3, Young's modulus $E^s = 1.0 \times 10^6$ Pa and Poisson's ratio $\nu^s = 0.3$. The deformation of the piston is very small; hence, the piston can be viewed as a "rigid" body. The fluid and solid domains are discretized using irregular T4 elements, as plotted in Fig. 4. In order to study the convergence properties of 3D IS-FEM in space, the fluid domain is discretized by a series of meshes as tabulated in Table 1.

The solid piston is forced to move inside the fluid tunnel along the x_2 direction with a constant velocity v^s_2. Consequently, a laminar fluid flow will be induced due to the
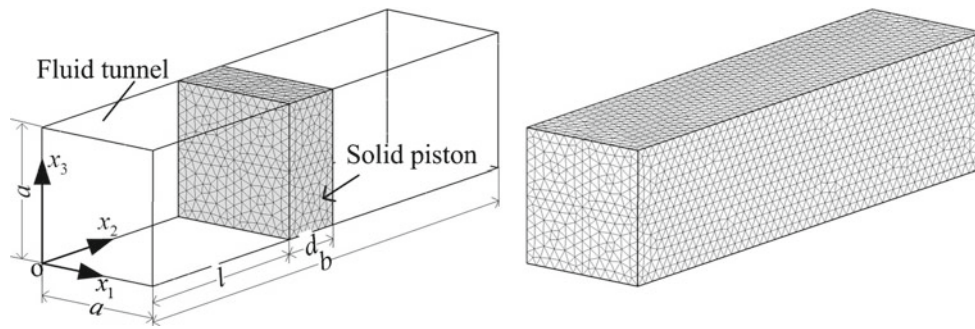
Fig. 4 Example 5.1: a moving piston in a tunnel. *Left* fluid domain and T4 mesh for solid piston; *right* T4 mesh for the fluid domain

Table 1 Meshes for Example 5.1

	Meshes for fluid				Meshes for solid	
	MS(1)	MS(2)	MS(3)	MS(4)	MS(i)	MS(ii)
N_{nd}	2,745	10,956	43,754	182,819	1,383	135
N_{ele}	12,674	56,844	239,925	104,0793	6,081	400
h	1/16	1/24	1/40	1/64	h/24	h/8

N_{nd} number of nodes, N_{ele} number of elements, h average element size

motion of the solid piston. The I.C. and B.C. for the fluid and solid piston are given as follows.

V.B.C. for fluid: slip boundary condition on $x_1^f = 0$, $x_1^f = a$, $x_3^f = 0$ and $x_3^f = a$;

P.B.C. for fluid: $p^f = 0$ on $x_2^f = 0$ and $x_2^f = b$;
I.C. for fluid: $^0v_i^f = 0$, $(i = 1, 2, 3)$.
V.B.C. for solid: $v_1^s = 0$, $v_3^s = 0$ and $v_2^s = 2.0$ m/s on $x_1^s = 0$, $x_1^s = a$, $x_3^s = 0$ and $x_3^s = a$.
I.C. for solid: $^0v_i^s = 0$, $(i = 1, 2, 3)$.

Under the above boundary and initial conditions, the exact velocity solution of the fluid flow can be determined as $v_1^f = v_3^f = 0$ and $v_2^f = 2.0$ m/s. Using the proposed IS-FEM procedure and the standard FEM discretization for the fluid and solid parts, one can easily solve this simple 3D FSI problem and implement the convergence and accuracy studies. Figure 5 shows the contour plots of the velocity component v_2^f and the pressure p^f with the streamlines on the slice surfaces $x_1^f = a/2$ and $x_3^f = a/2$ at the time $t = 0.6$ s. The
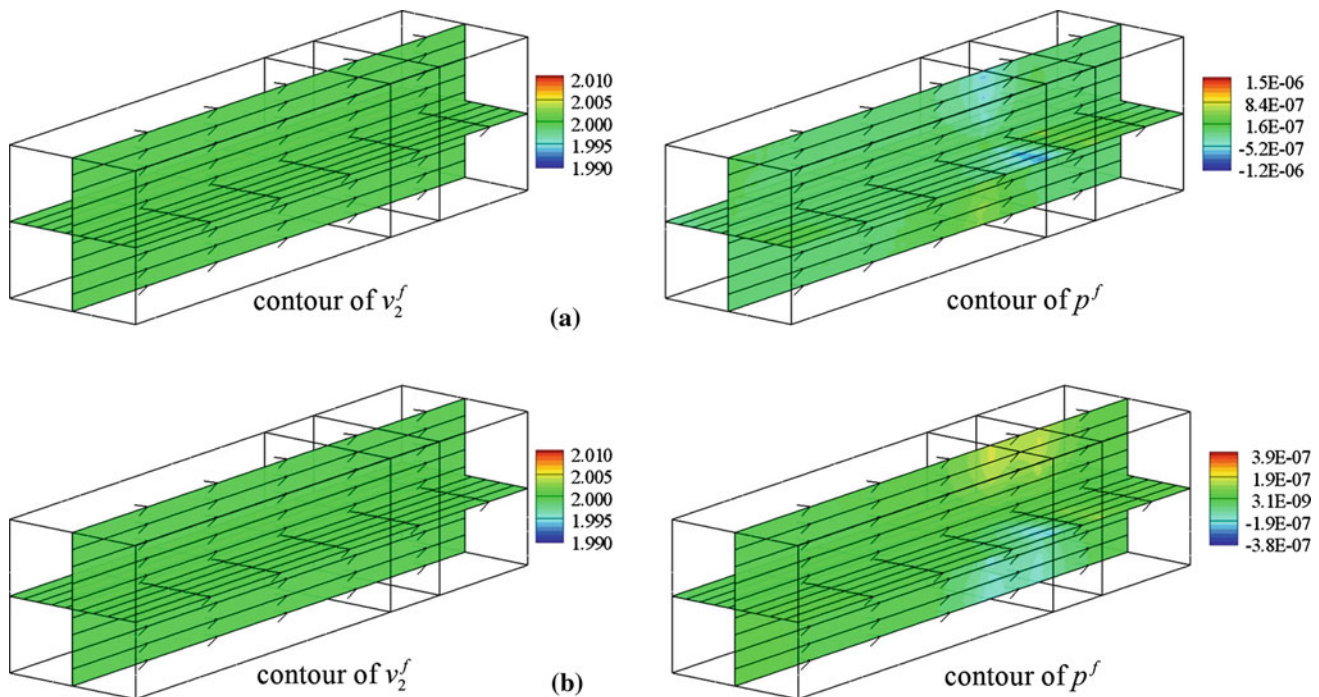
Fig. 5 Results for Example 5.1: contour plots of the fluid velocity component and pressure with streamlines on the slice surfaces at the time t=0.6 s solved using meshes **a** MS(3) and MS(ii) and **b** MS(4) and MS(i)
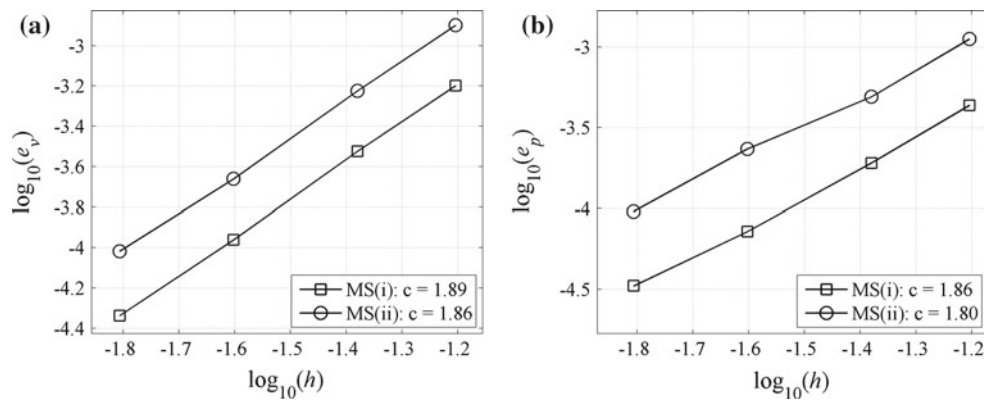
Fig. 6 Spatial convergence properties based on Example 5.1 for **a** fluid velocity solution and **b** pressure solution (c: convergence rate; h: average element size)

streamlines and the velocity contour plots clearly show the stable laminar flow solved using different combinations of the solid and fluid meshes.

Notably, Fig. 5b shows that, when using quite small mesh size ratio $h^f / h^s = 1/8$, the proposed IS-FEM still works well and can produce the stable fluid velocity and pressure solutions with no numerical artifact and unphysical oscillations observed.

The spatial convergence and accuracy studies are carried out in virtue of the errors in the fluid velocity and pressure solutions. The L2 error norms e_v and e_p in the fluid velocity and pressure solutions are defined by

$$e_v = \sqrt{\sum_{I=1}^{N_{DOF}} \left(v_i^{num} - v_i^{ref} \right)^2}; \quad e_p = \sqrt{\sum_{I=1}^{N_{nd}} \left(p_i^{num} - p_i^{ref} \right)^2}.$$
(34)

In this example, the reference solution v_i^{ref} is given by the exact solution. All the errors are calculated at the time $t = 0.6$ s.

Figure 6 shows that the convergence rates for the fluid velocity solutions are 1.88 using the finer solid mesh MS(i) and 1.84 using the coarser solid mesh MS(ii), and the convergence rates for the fluid pressure solutions are 1.86 using the finer solid mesh MS(i) and 1.80 using the coarser solid mesh MS(ii). The convergence rates are very close to the theoretical convergence rate 2.0. One can clearly observe that the coarse solid mesh degrades the convergence rate and the computation accuracy.

5.2 3D lid-driven cavity flow with a hyperelastic solid wall (Example 5.2)

A 3D lid-driven cavity fluid flow with an incompressible hyperelastic solid wall is analyzed in this example as illustrated in Fig. 7. The length and the height of the fluid domain are $l = 2.0$ m, and the thickness is $b = 0.2$ m. The solid

wall is located at the bottom surface of the fluid domain, with the length $l = 2.0$ m, the thickness $b = 0.2$ m and the height $a = 0.5$ m. The properties of the fluid are given as $\rho^f = 1.0$ kg m^3 and $\mu^f = 0.2$ kg (m s)$^{-1}$. In this example, the constitutive model of the solid wall is set to be the incompressible neo-Hookean material, with the material constant $A_{10} = 0.1$ kg $\left(\text{m s}^2 \right)^{-1}$, $A_{01} = 0$ and $\kappa = 0$.

This example has been solved in 2D cases under plane strain condition as a benchmark problem to examine the interactions between the incompressible viscous fluid and the hyperelastic nonlinear solid, using immersed-type methods and the ALE method [23,25,47]. In order to compare the 3D solution with the reported 2D plane strain solution, the proper boundary conditions for the fluid and solid should be enforced. Under the following boundary conditions, the 3D solution in the $x_1 x_2$ plane is comparable with the 2D plane strain solution.

V.B.C. for fluid: $v_1^f = \bar{v}$, $v_2^f = v_3^f = 0$ on the top lid surface $x_2 = l$; non-slip conditions on four surfaces $x_1 = 0$, $x_1 = a$, and $x_2 = 0$; and $v_3^f = 0$ on two surfaces $x_3 = 0$ and $x_3 = b$. The fluid lid velocity $\bar{v}$ is defined as follows in order to remove the singularities at the left-top and right-top corners of the fluid field,

$$\bar{v} = \begin{cases} \sin^2 \left(\pi x_1 / 0.6 \right) & x_1 \in [0.0, \ 0.3] \\ 1.0 & x_1 \in (0.3, \ 1.7) \\ \sin^2 \left(\pi \left(x_1 - 2.0 \right) / 0.6 \right) & x_1 \in [1.7, \ 2.0] \end{cases}$$
(35)

P.B.C. for fluid: $p^f = 0$ on the line $(l/2, 0, x_3)$.
*I.C. for fluid:* $v_i^f = 0$ and $p^f = 0$ at the time $t = 0$.
V.B.C. for solid: $v_i^s = 0$ $(i = 1, 2, 3)$ on four surfaces $x_1 = 0$, $x_1 = a$, and $x_2 = 0$; and $v_3^s = 0$ on two surfaces $x_3 = 0$ and $x_3 = b$.
I.C. for solid: $v_i^s = 0$ and $p^f = 0$ at the time $t = 0$.

Both the fluid and solid domains are discretized irregularly using T4 elements, as illustrated in Fig. 7. Several sets of the fluid and solid meshes are employed for the spatial convergence and accuracy studies, as listed in Table 2. The

Fig. 7 Example 5.2: 3D lid-driven cavity flow with a hyperelastic solid wall

T4 mesh for solid　　　　T4 mesh for fluid
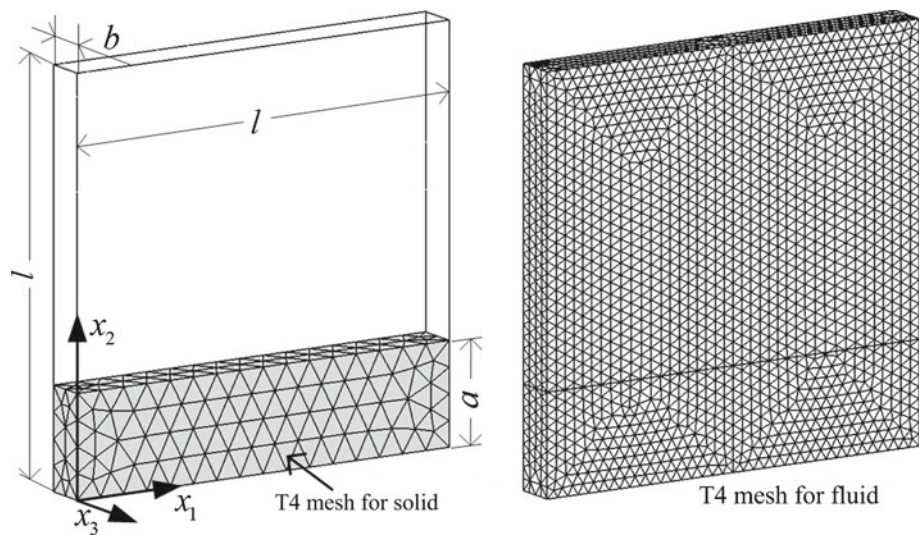
Table 2 Meshes for Example 5.2

N_{nd} number of nodes, N_{ele} number of elements, h average element size

		Meshes for fluid							Meshes for solid	
		MS(1)	MS(2)	MS(3)	MS(4)	MS(5)	MS(6)	MS(7)	MS(i)	MS(ii)
	N_{nd}	1,392	4,603	7,626	9,413	13,172	18,416	218,636	240	1,083
	h	1/20	1/30	1/36	1/40	1/44	1/50	1/160	1/16	1/30

deformation of the solid wall is analyzed using Selective S-FEM. The cavity fluid flow driven by the moving lid produces the FSI force applied on the top surface of the solid wall and causes the soft solid wall to deform largely. The deformation continues until the steady state is reached where the FSI force and the internal force of the solid are in balance. In this example, the FSI system is considered to have reached the steady state if the kinematics energy of the solid wall is $\left\| {}^n v_i^s \right\|^2 \le 10^{-4}$. The fluid velocity and pressure fields and the deformed mesh of the solid are visualized in Fig. 8. The velocity amplitude is calculated by $v = \left(v_1^2 + v_2^2 + v_3^2 \right)^{1/2}$. Figure 8 evidently shows the fluid solutions calculated using the coarser fluid and solid meshes still agree reasonably well with those using finer meshes. In particular, the employment of much finer fluid mesh than solid mesh, i.e., the mesh size ratio h^f / h^s is at very small value of $1/10$ (see Fig. 8c), the proposed method is still quite stable and does not lead to numerical artifact solution. No unphysical velocity and pressure solutions are observed, which has been reported in [23].

Under the properly prescribed boundary conditions, the motions of the fluid and solid particles remain mainly in the $x_1 x_2$ plane, depicted by the iso-surfaces of the fluid velocity at the values $v = 0.05$, $v = 0.20$ and $v = 0.25$ m/s in Fig. 8. The planar motions of the fluid and solid particles satisfy essentially the plane strain assumption. As such, the solutions in this 3D FSI problem can be compared with the referenced 2D FSI problem under plane strain condition.

The comparisons are shown in Fig. 9 with the 2D reference solutions found in the references [23,25,47], respectively. The profiles of the 3D FSI solutions at the steady state are given by the nodes located on the slice surface $x_3 = b/2$. There is a good agreement between the 2D and 3D FSI solutions.

Spatial convergence studies are carried out using the solid mesh MS(ii) and the fluid meshes MS(k), (k = 1 to 6). The L2 error norms in the fluid velocity and pressure solutions are given in Fig. 10. The reference solutions v_i^{ref} and p^{ref} in Eq. (34) are computed using the very fine fluid mesh MS(7) and the solid mesh MS(ii). In as much as the fluid and solid meshes are all irregular meshes, the nodal solutions of the fluid velocity and pressure on the meshes MS(k), (k = 1 to 6) are obtained by the linear interpolations from the reference nodal solutions on MS(7). The spatial convergence rate for the fluid velocity and pressure solutions are 1.85 and 1.61.

5.3 Sphere falling inside fluid under gravity (Example 5.3)

A solid sphere falling under the gravity inside a cylinder tank filled with incompressible viscous fluid is analyzed in this example. The sphere starts falling from the state of rest under the gravity force. During the falling process, the FSI force is applied on the sphere, including buoyant force, viscous force and others. The sphere accelerates from the initial rest state due to the imbalance between the gravity and FSI forces.
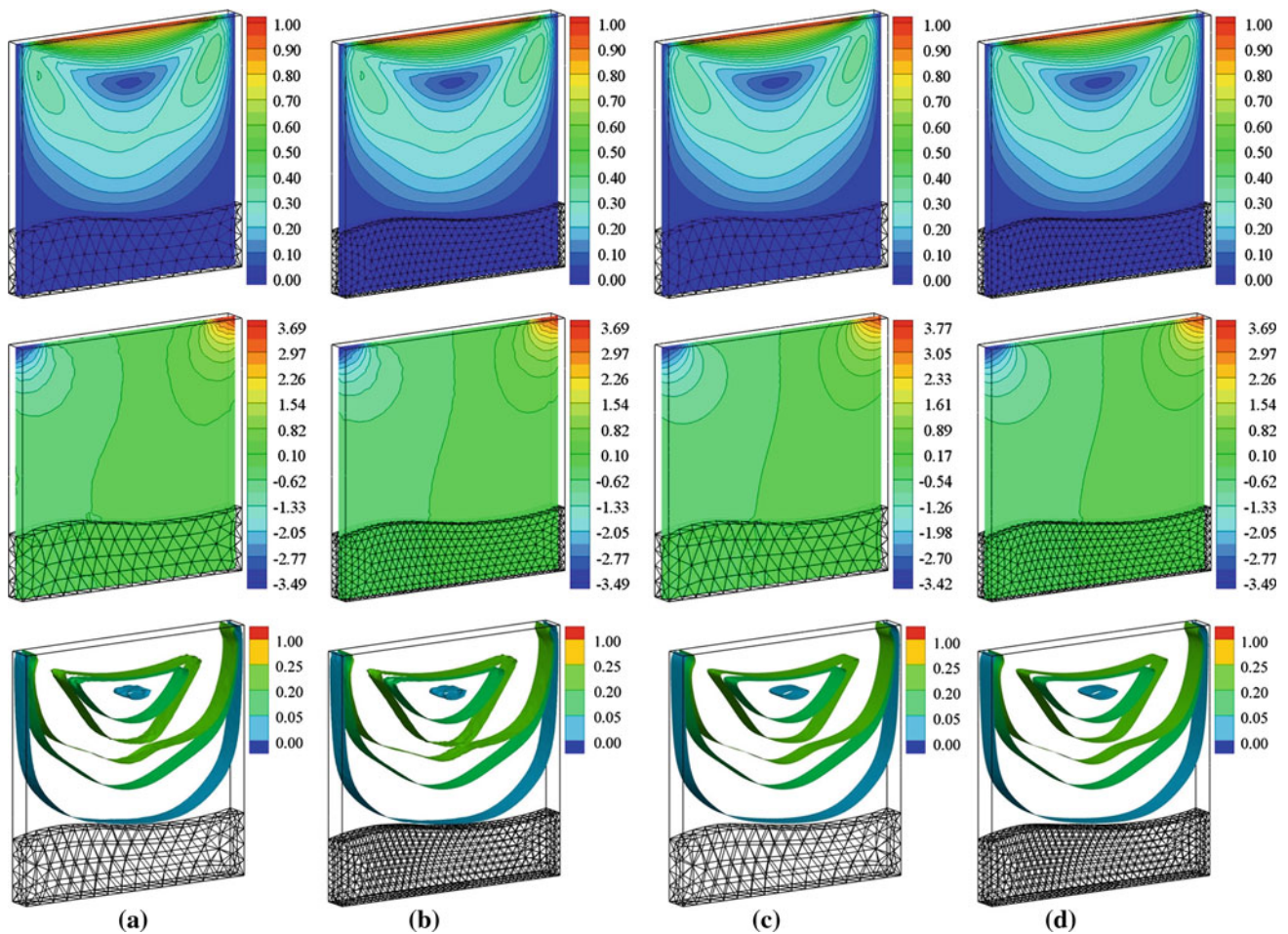
Fig. 8 Results for Example 5.2 solved using meshes: **a** MS(3) and MS(i); **b** MS(3) and MS(ii); **c** MS(7) and MS(i); **d** MS(7) and MS(ii) (*top row* slice contour plots of the fluid velocity amplitude; *mid row* slice contour plots of the fluid pressure; *bottom row* iso-surfaces of the fluid velocity at 0.05, 0.2 and 0.25 m/s)
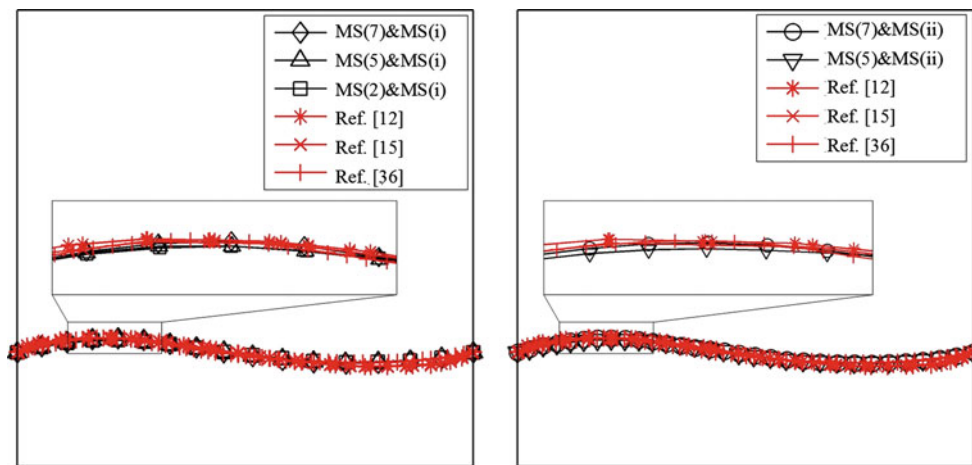
Fig. 9 Profiles of the deformed hyperelastic wall solved using different meshes

As the velocity increases, the FSI force becomes larger and larger and finally balances the gravity force leading to the terminal settling velocity $\bar{v}$.

In this example, the diameter of the solid sphere is given as D and the diameter of the cylinder tank is 5D. The height of the tank is H, as shown in Fig. 11. The values
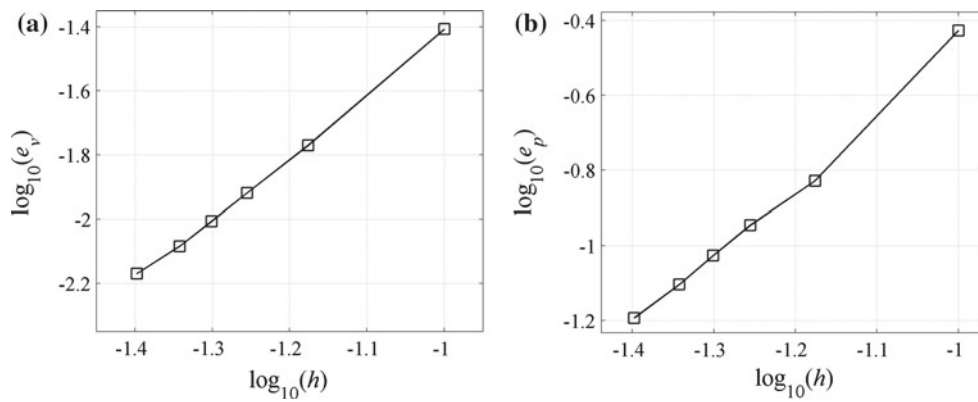
Fig. 10 Spatial convergence properties of Example 5.2 in **a** fluid velocity solutions and **b** pressure solutions (h: average element size)
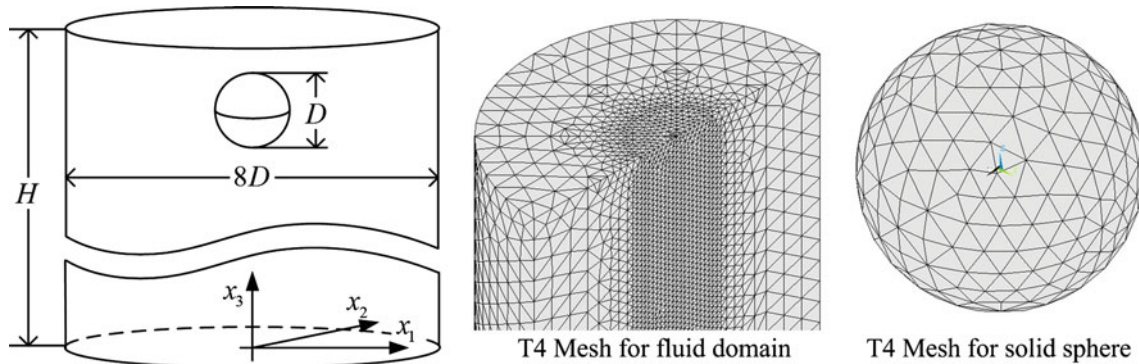
Fig. 11 Example 5.3: sphere falling inside the fluid medium under gravity (only T4 mesh for half of the fluid domain is plotted)

of D and H are given in Table 3. The fluid is the water at 25 °C, with the properties: $\rho^f = 997.13\,\mathrm{kg\,m^{-3}}$ and $\mu^f = 8.91 \times 10^{-4}\,\mathrm{kg\,(m\,s)^{-1}}$. Three experiments with different solid spheres are tested, and the corresponding material properties and sizes are tabulated in the Table 3. The terminal settling velocities for the three cases have been reported in experiments [48]. In terms of the experimental data, the Reynolds number can be determined according to the falling velocity and the diameter D. In both the experiment and numerical simulation, the fluid in the tank is initially unperturbed and in hydrostatic state. The Young's modulus and Poisson ratio of the spheres in the three numerical simulations are given as $E^s = 1 \times 10^4\,\mathrm{kg\,(m\,s^2)^{-1}}$ and $\upsilon^s = 0.3$. The deformations of the solid spheres are very small, so the spheres can be viewed as essentially "rigid". Therefore this, for all practical purposes, becomes a fluid–particle interaction (FPI) problem. Much has been accomplished in computation for FPI problems during the period 1996–2001. Reference [49] reported the first 3D finite element FPI computation, where the number of particles ranged from 2 to 5, and particle–particle interactions (collisions) were taken into account. The reference [50] reported the 3D computations with the number of particles reaching 100 for the first time, and reference [51] reported the 3D computations where the

number of particles reached 1,000 for the first time. Reference [52] is where methods were introduced for FPI computations in spatially-periodic 3D domains, results were reported with the number of particles reaching 128, and an extensive study was presented focusing on the number particle needed in a periodic cell.

The initial distance between the center of the spheres and the top surface of the tank is set at 2D. The boundary and initial conditions are given as follows:

*V.B.C for fluid*: $v_i^f = 0$ ($i = 1, 2, 3$) on all surfaces of the tank (e.g., non-slip condition);
P.B.C for fluid: $p^f = 0$ on the surface $x_3 = 0$;
I.C. for fluid: $v_i^f = 0$ ($i = 1, 2, 3$);
V.B.C for solid: no velocity boundary conditions are applied;
I.C. for solid: $v_i^f = 0$ ($i = 1, 2, 3$).

The acceleration of the gravity is $g = 9.8\,\mathrm{m\,s^{-2}}$.

For the Case #1, the cylindrical fluid domain and the solid sphere are discretized using two sets of fluid and solid meshes: MS(1) irregular T4 meshes with 56248 nodes for the fluid and 514 nodes for the solid, as shown in Fig. 11; MS(2) irregular T4 meshes with 185329 nodes for the fluid and 1534 nodes for the solid. The Case #2 and Case #3 employ MS(3):

Table 3 Experimental set-up of sphere falling inside the fluid medium under gravity

	Density ρ^s $(\mathrm{kg\,m^{-3}})$	Diameter D (m)	Height of tank H (m)	Settling velocity $\bar{v}$	Reynolds number $Re = (\rho^f \bar{v} D)/\mu^f$
Case #1	2,560	5×10^{-4}	10 D	0.0741	41
Case #2	7,670	2×10^{-3}	30 D	0.636	1,400
Case #3	7,700	4×10^{-3}	30 D	0.973	4,300
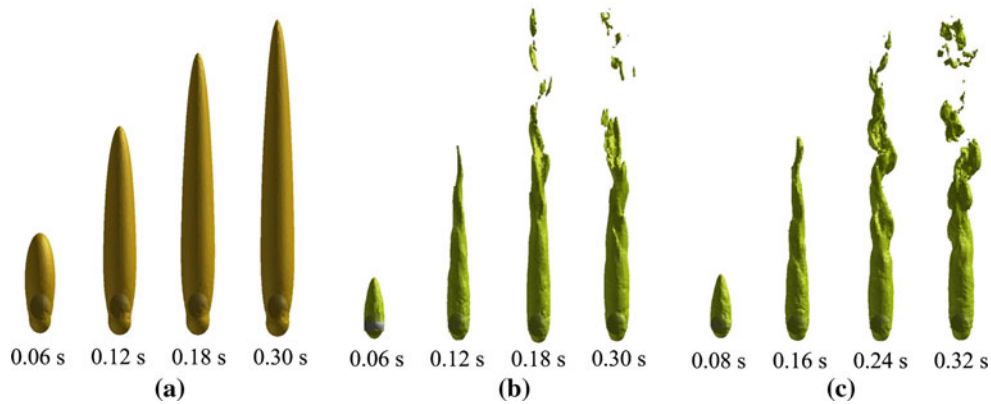
Fig. 12 Results for Example 5.3. Snapshots of iso-surfaces of v_3: **a** $v_3 = -0.01$ m/s for Case #1; **b** $v_3 = -0.2$ m/s for Case #2; **c** $v_3 = -0.2$ m/s for Case #3

irregular T4 meshes with 367461 nodes for the fluid and 1534 nodes for the solid.

The results of the numerical simulations are visualized in Figs. 12 and 13. Figure 12 shows the snapshots of the iso-surfaces of the fluid velocity component v_3 at the values of $v_3 = -0.01$, $v_3 = -0.2$ and $v_3 = -0.2 \, hboxm/s$ for the three cases, respectively. Figure 13 plots the contours of the fluid velocity component v_z and the fluid pressure on the slice plane $x = 0$ at the settling stage. For Case #1, the maximum Reynolds number at the settling stage is a small value at $Re = 41$. As such, the fluid flow around the sphere always remains axisymmetric about the vertical axis passing through the center of the sphere. In this case, the trajectory is vertical and produces a stable wake flow, which can be clearly observed in Figs. 12a and 13a. The pressure contour plots in Fig. 13a clearly show that, in Case#1 the movement of the sphere only perturbs the fluid hydrostatic pressure field slightly in the regions near the solid sphere. In the far-zone of the wake region the fluid pressure field still retains the characteristics of the hydrostatic pressure. The Reynolds numbers for Case #2 and Case #3 at the settling stage are relatively larger at $Re = 1,400$ and $Re = 4,300$, respectively. In the short period after the sphere begins falling, due to the small falling velocity the instantaneous Reynolds number is small. Hence, the fluid flow around the sphere in the wake region is fairly axisymmetric, as shown in the Fig. 12b at $t = 0.06$ s and Fig. 12c at $t = 0.08$ s, respectively. Once the falling velocity and the associated Reynolds number increase to sufficiently large values, the fluid wake flow becomes unsteady and cannot keep to the

axisymmetric behavior, as illustrated in Figs. 12b and 12c. One can observe that at the settling stage the wake flow of Case #3 as shown in Figs. 12c and 13c is more unsteady than that of Case #2 as depicted in Figs. 12b and 13b. This is attributed to the much higher Reynolds number at the settling stage for Case #3. The pressure fields for Case #2 and Case #3, as depicted in Fig. 13b, c, are significantly disturbed.

The histories of the average velocity v_3 of the solid sphere are compared with the experimental results in Fig. 14. The figure shows that for all the three cases the terminal settling velocities achieved by the numerical simulations display good agreements with the experimental results when fine meshes are used. It clearly demonstrates that the proposed IS-FEM scheme provides the valid FSI force, which is in final equilibrium with the gravity force.

5.4 Flow passing a cylinder with a flexible flag (Example 5.4)

In two dimensional FSI analysis, a benchmark FSI problem of a cylinder with a flexible flag in the downstream side is often used to verify the numerical FSI scheme [53,54]. In this example, this benchmark is extended to three dimensions as illustrated in Fig. 15. The fluid domain is a cuboid channel with the geometry parameters given as: $L = 2.5$ m, $W = 0.02$ m and $H = 0.41$ m. The geometry parameters of the solid cylinder and flag are: $w = 0.05$ m, $l = 0.35$ m and $h = 0.02$ m. The location of the cylinder is determined by $c = 0.2$ m. The inflow velocity $\bar{v}^f(t)$ is prescribed at the left
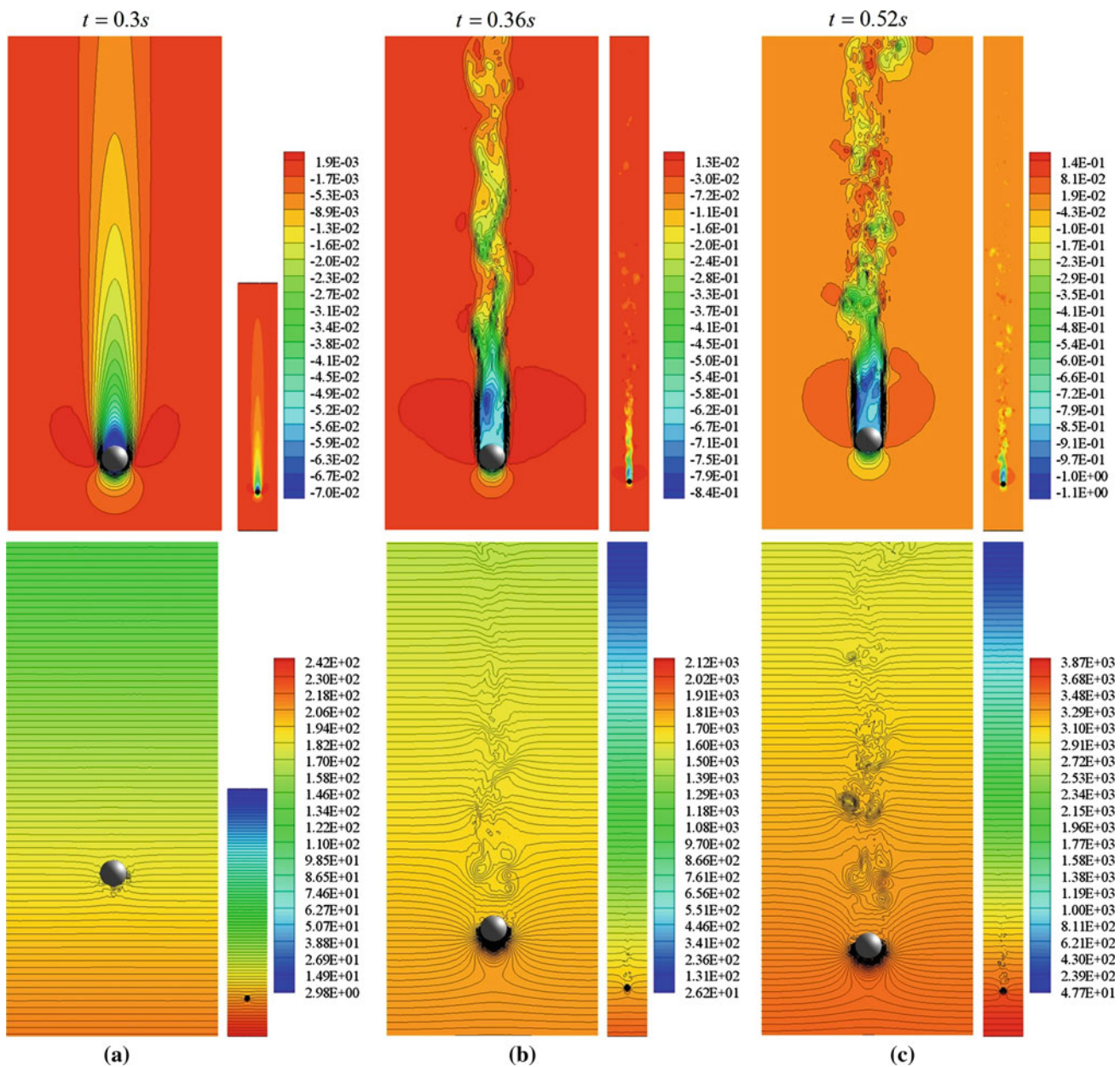
Fig. 13 Results for Example 5.3. Snapshots of contours of the fluid velocity v_3 (*top row*) and the fluid pressure (*bottom row*) in the slice plane $x_1 = 0$: **a** Case #1; **b** Case #2; **c** Case #3

surface $x_1 = 0$ with the following parabolic profile

$$\bar{v}^f(t) = \begin{cases} \bar{v}\dfrac{1-\cos(\pi t/2)}{2} & t < 2.0 \\ \bar{v} & t \geq 2.0 \end{cases}$$

where $\bar{v} = 1.5\bar{U}x_2(H - x_2)/(H/2)^2$. $\qquad$ (36)

The mean inflow velocity is $\bar{U}$ when the inflow is steady after about $t = 2.0$ s.

Using the same geometric model of the fluid and solid domains, three cases examined in [53] are tested in this exam-

ple with the different solid material properties and inflow velocity, as tabulated in Table 4.

The calculation starts at the rest state of the fluid and solid for all the cases. And the boundary conditions are prescribed as follows:

V.B.C. for fluid: $^\tau v_1^s = \bar{v}^f(t)$, $^\tau v_2^s = {^\tau v_3^s} = 0$ at $x_1 = 0$; $^\tau v_i^s = 0$ $(i = 1, 2, 3)$ at $x_2 = 0$ and $x_2 = H$; $^\tau v_3^s = 0$ at $x_3 = 0$ and $x_2 = W$;

P.B.C. for fluid: $^\tau p^f = 0$ at $x_1 = L$;

Fig. 14 History of the falling velocity v_3 **a** Case #1; **b** Case #2; **c** Case #3
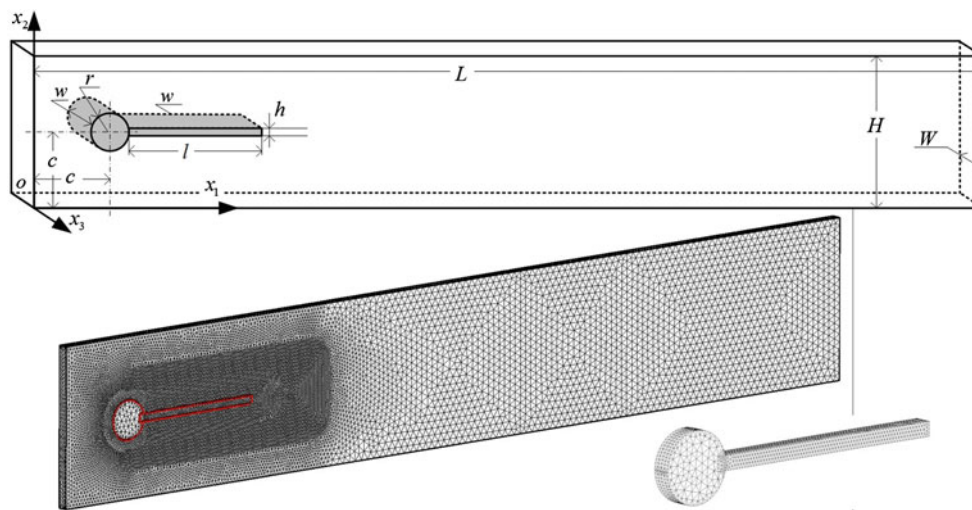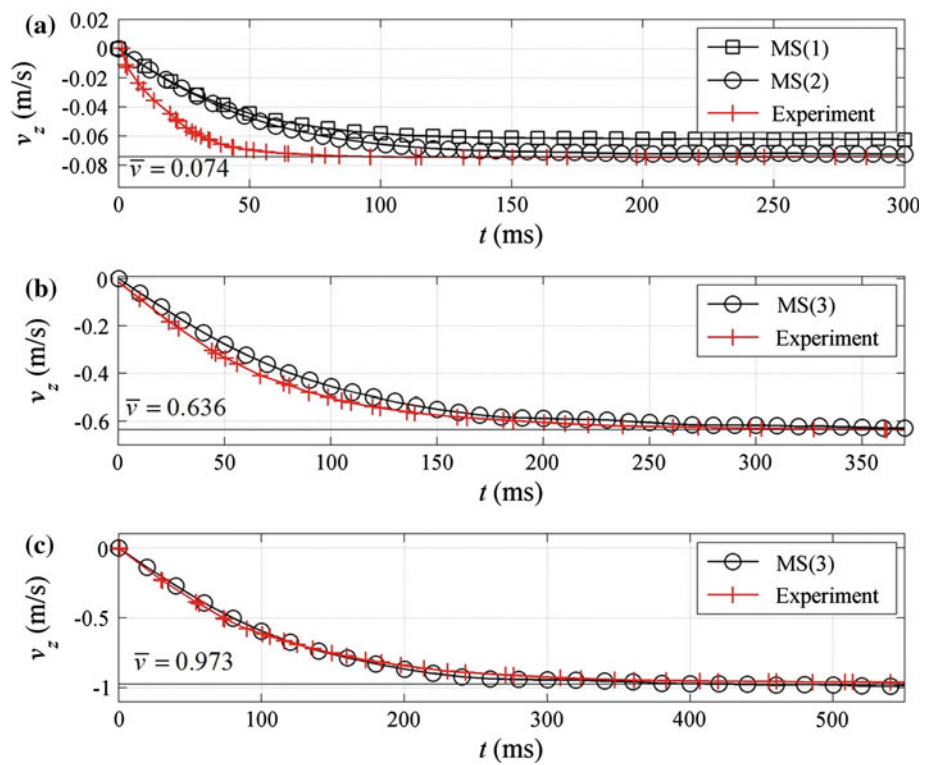
Fig. 15 Example 5.4: fluid flow past a cylinder with a flag

Table 4 Problem set-ups for Example 5.4

Parameter	FSI-1	FSI-2	FSI-3
ρ^s 10^3 kg m^{-3}	1	10	1
v^s	0.4	0.4	0.4
μ^s 10^6 kg (m s^2)$^{-1}$	0.5	0.5	2.0
ρ^f 10^3 kg m^{-3}	1	1	1
μ^f kg (m s)$^{-1}$	1	1	1
$\bar{U}$ m s^{-1}	0.2	1	2
$Re = 2\rho^f r\bar{U}/\mu^f$	20	100	200

V.B.C. for solid: $^\tau v_i^s = 0$ $(i = 1, 2, 3)$
if $\sqrt{(x_1 - c)^2 + (x_2 - c)^2} = r$.

The fluid domain is discretized by the irregular T4 mesh with 145344 nodes and the solid domain is discretized by the irregular T4 meshes with 2084 nodes. The average mesh size for the solid flag is approximately $h^s = h/4$, and the average mesh size for the fluid domain in the vicinity of the flag is $h^f = h/8$ as shown in Fig. 15. FS-FEM-T3 is employed for analyzing the large deformation of the flexible flag. The displacement solution at the point A (0.6, 0.2, 0.01) on the right

Fig. 16 Results for Example 5.4 (case FSI-1): the contour plots of the fluid pressure and streamlines on the slice $x_3 = W/2$ at the steady state
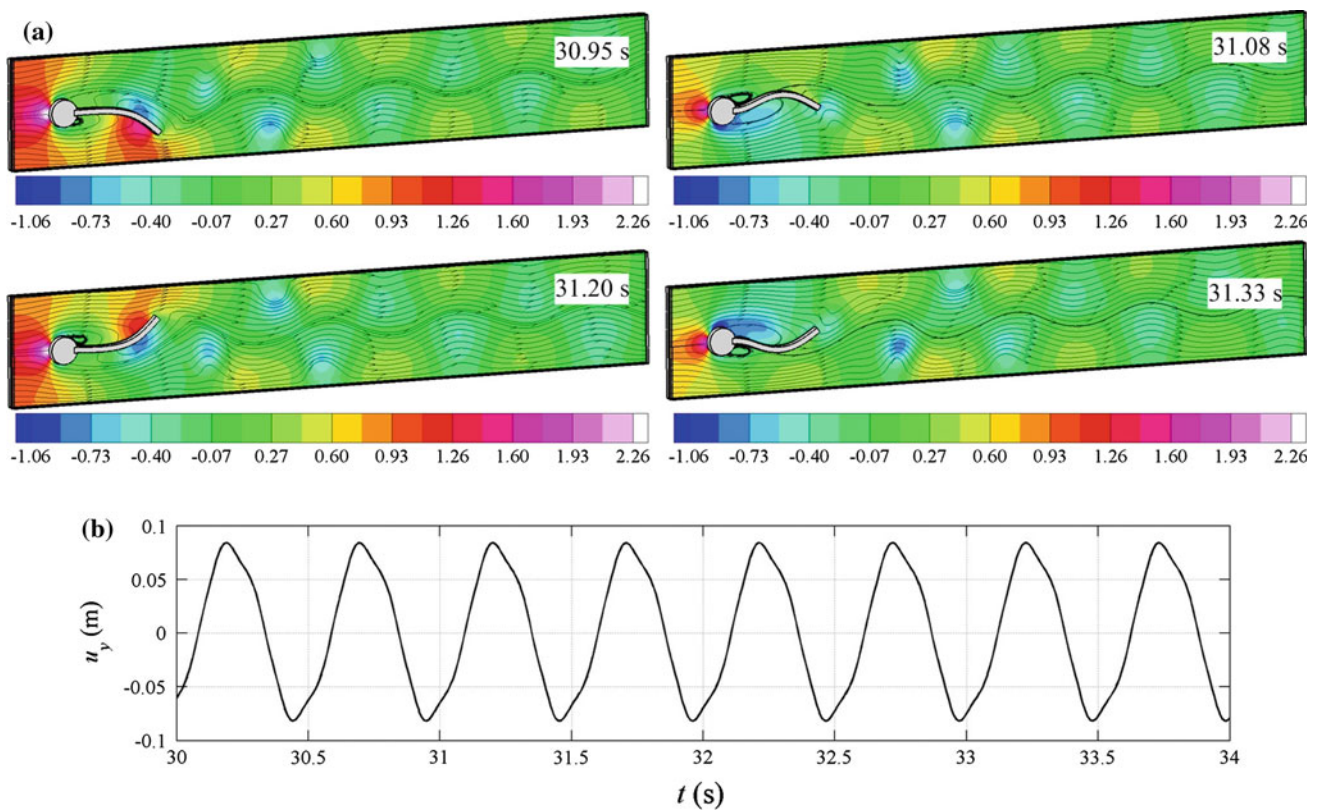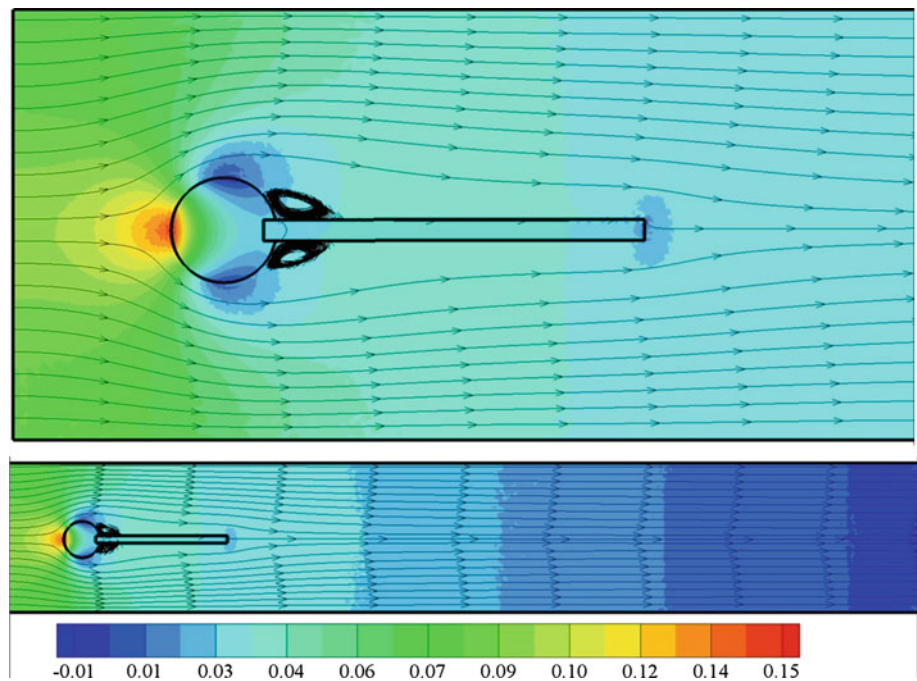
Fig. 17 Results for Example 5.4 (case FSI-2) **a** snapshots of the fluid pressure contours and streamlines on the slice $x_3 = W/2$; **b** history of displacement component of the point A

tip of the flag is measured and compared with the reported reference solutions.

Due to the low Reynolds number Re $= 20$ for the case FSI-1, it finally results in a steady state solution. At the steady state

the FSI force applied on the deformed flag are in balance with the internal force, and u_2^s of the point A takes on a constant value $u_2^s = 8.314 \times 10^{-4}$ m, which agrees very well with the reference solution $u_2^s = 8.209 \times 10^{-4}$ m [53]. The contour
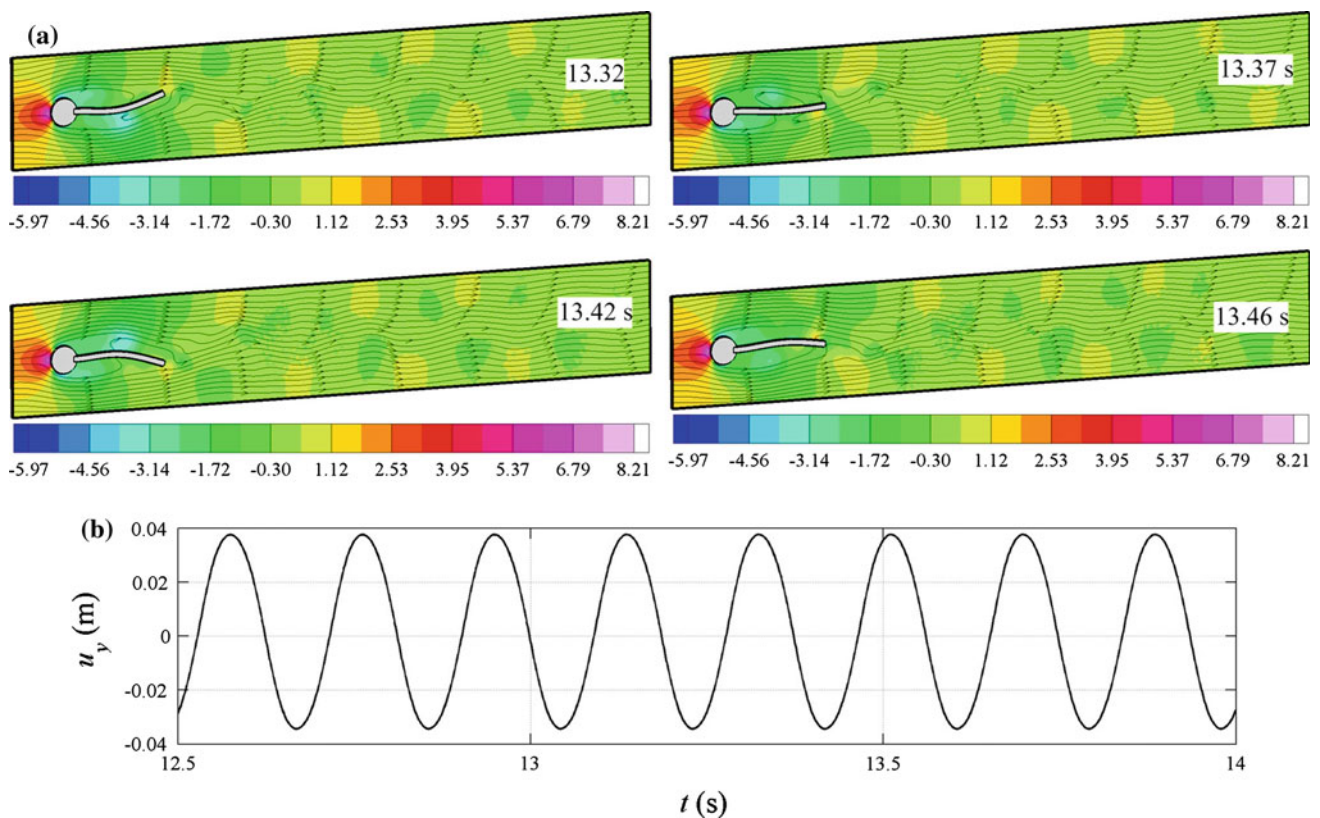
Fig. 18 Results for Example 5.4 (case FSI-3) **a** snapshots of the fluid pressure contours and streamlines on the slice $x_3 = W/2$; **b** history of displacement component of the point A

of the fluid pressure field with streamlines at the steady state is plotted in Fig. 16. The Reynolds number of the case FSI-2 is Re = 100, hence, the system settles into a large-amplitude self-excited oscillation following the initial transient quiescent period. The oscillating flag produces a regular vortex pattern that is advected along the channel, which is shown in Fig. 17. Figure 17a provides the snapshots of the pressure contour with instantaneous streamlines in one period of the flag oscillation. The vertical tip displacement at point A in is $u_2^s \approx 0.001 \pm 0.083$ m, fairly comparable with the reference solution $u_2^s \approx 0.00123 \pm 0.0806$ m. The histories of u_2^s at the point A are given in Fig. 17b. The period of the oscillation is $T \approx 0.52$ s. The case FSI-3 with Re = 200 also develops a periodically oscillating fluid flow with regular vortex pattern similar to the case FSI-2, shown in Fig. 18. The period of the FSI-3 is approximately $T \approx 0.19$ s. The vertical tip displacement at point A is $u_2^s \approx 0.001 \pm 0.036$ m, agreeing well with the reference solution $u_2^s \approx 0.00148 \pm 0.03438$ m.

6 Conclusions

In this work, 3D FSI problems are successfully solved by the proposed immersed smoothed finite element method

(IS-FEM). The IS-FEM is a kind of partitioned approach, consisting of three main modules: semi-implicit Galerkin procedure based on CBS scheme for the transient incompressible viscous flows; S-FEM using explicit time integration for dynamics analysis of the nonlinear solids; immersed methodology for evaluating FSIs based on a set of novel Lagrangian fictitious fluid mesh. The Lagrangian fictitious fluid mesh coincides with the moving solid mesh, in which the geometry information can be naturally achieved with ease. The method is implemented via the simplest four-node tetrahedral element, which has advantages in simple pre-processing, adaptive analysis and convenient data exchange of the velocity and pressure fields between the Eulerian fluid mesh and the Lagrangian solid mesh. Numerical examples are compared with the reported reference numerical and experimental results leading to the following conclusions:

(1) The moving boundary in the fluid flow can be tracked without any difficulty using the immersed methodology in 3D IS-FEM. No sophisticated re-meshing is required.

(2) Good agreements with the published reference numerical and experimental results verify the validity and accuracy of the 3D IS-FEM.

(3)   IS-FEM possesses the second order convergence rate for the fluid velocity and pressure in space, which arise from the Galerkin procedures of CBS and S-FEM schemes.

(4)   No reported "leaking" phenomena and unphysical solutions are observed while employing both coarse and fine fluid mesh. The stability of 3D IS-FEM is not affected for a wide range of the size ratio (up to $h^f/h^s = 1/10$ is examined in this research).

(5)   It is worthy to note that the calculation of FSI force only needs the fluid pressure being interpolated, and the implementation of the nodal FSI velocity condition can be interpolated easily from the solid velocity field. All these interpolations are performed by simple linear interpolation based on T4 element.

(6)   The proposed operations in Sect. 4 are general algorithms, and provide possibility and flexibility for users to choose other fluid solvers, e.g., finite volume method (FVM) and finite difference method (FDM), and so on.

References

1. Donea J, Guiliani S, Halleux JP (1982) An arbitrary Lagrangian-Eulerian finite-element method for transient dynamic fluid structure interactions. Comput Methods Appl Mech Eng 33:689–723. doi:10.1016/0045-7825(82)90128-1

2. Hu HH, Patankar NA, Zhu MY (2001) Direct numerical simulations of fluid-solid systems using the arbitrary Lagrangian-Eulerian technique. J Comput Phys 169:427–462. doi:10.1006/jcph.2000.6592

3. Liu WK, Chang H, Chen JS, Belytschko T (1988) Arbitrary Lagrangian-Eulerian Petrov-Galerkin finite-elements for nonlinear continua. Comput Methods Appl Mech Eng 68:259–310. doi:10.1016/0045-7825(88)90011-4

4. Bazilevs Y, Calo VM, Zhang Y, Hughes TJR (2006) Isogeometric fluid–structure interaction analysis with applications to arterial blood flow. Comput Mech 38:310–322. doi:10.1007/s00466-006-0084-3

5. Tezduyar TE, Aliabadi SK, Behr M, Mittal S (1994) Massively-parallel finite-element simulation of compressible and incompressible flows. Comput Methods Appl Mech Eng 119:157–177. doi:10.1016/0045-7825(94)00082-4

6. Mittal S, Tezduyar TE (1995) Parallel finite-element simulation of 3D incompressible flows–fluid–structure interactions. Int J Numer Methods Fluids 21:933–953. doi:10.1002/fld.1650211011

7. Kalro V, Tezduyar TE (2000) A parallel 3D computational method for fluid–structure interactions in parachute systems. Comput Methods Appl Mech Eng 190:321–332. doi:10.1016/S0045-7825(00)00204-8

8. Tezduyar TE, Sathe S, Keedy R, Stein K (2006) Space–time finite element techniques for computation of fluid–structure interactions. Comput Methods Appl Mech Eng 195:2002–2027. doi:10.1016/j.cma.2004.09.014

9. Tezduyar TE, Sathe S (2007) Modelling of fluid–structure interactions with the space–time finite elements: solution techniques. Int J Numer Methods Fluids 54:855–900. doi:10.1002/fld.1430

10. Tezduyar TE, Sathe S, Pausewang J, Schwaab M, Christopher J, Crabtree J (2008) Interface projection techniques for fluid–struc-ture interaction modeling with moving-mesh methods. Comput Mech 43:39–49. doi:10.1007/s00466-008-0261-7

11. Takizawa K, Tezduyar TE (2011) Multiscale space–time fluid–structure interaction techniques. Comput Mech 48:247–267. doi:10.1007/s00466-011-0571-z

12. Bazilevs Y, Calo VM, Hughes TJR, Zhang Y (2008) Isogeometric fluid–structure interaction: theory, algorithms, and computations. Comput Mech 43:3–37. doi:10.1007/s00466-008-0315-x

13. Peskin CS (1972) Flow patterns around heart valves: a numerical method. J Comput Phys 10:252–271. doi:10.1016/0021-9991(72)90065-4

14. Peskin CS (1977) Numerical analysis of blood flow in the heart. J Comput Phys 25:220–252. doi:10.1016/0021-9991(77)90100-0

15. Mohd-Yusof J (1997) Combined immersed-boundary/b-Spline methods for simulations of flow in complex geometries CTR Annual Research Briefs, NASA Ames Research Center/Stanford University Center for Turbulence Research, Stanford, CA

16. Fadlun EA, Verzicco R, Orlandi P, Mohd-Yusof J (2000) Combined immersed-boundary finite-difference methods for three-dimensional complex flow simulations. J Comput Phys 161:35–60. doi:10.1006/jcph.2000.6484

17. Gilmanov A, Sotiropoulos F (2005) A hybrid Cartesian/immersed boundary method for simulating flows with 3D, geometrically complex, moving bodies. J Comput Phys 207:457–492. doi:10.1016/j.jcp.2005.01.020

18. Uhlmann M (2005) An immersed boundary method with direct forcing for the simulation of particulate flows. J Comput Phys 209:448–476. doi:10.1016/j.jcp.2005.03.017

19. Zhang L, Gerstenberger A, Wang X, Liu WK (2004) Immersed finite element method. Comput Methods Appl Mech Eng 193:2051–2067. doi:10.1016/j.cma.2003.12.044

20. Liu WK, Liu Y, Farrell D, Zhang L, Wang XS, Fukui Y, Patankar N, Zhang Y, Bajaj C, Lee J, Hong J, Chen X, Hsu H (2006) Immersed finite element method and its applications to biological systems. Comput Methods Appl Mech Eng 195:1722–1749. doi:10.1016/j.cma.2005.05.049

21. Zhang LT, Gay M (2007) Immersed finite element method for fluid–structure interactions. J Fluids Struct 23:839–857. doi:10.1016/j.jfluidstructs.2007.01.001

22. Lee TR, Chang YS, Choi JB, Kim DW, Liu WK, Kim YJ (2008) Immersed finite element method for rigid body motions in the incompressible Navier-Stokes flow. Comput Methods Appl Mech Eng 197:2305–2316. doi:10.1016/j.cma.2007.12.013

23. Wang XS, Zhang LT (2010) Interpolation functions in the immersed boundary and finite element methods. Comput Mech 45:321–334. doi:10.1007/s00466-009-0449-5

24. Zhang ZQ, Liu GR (2011) An immersed smoothed finite element method for fluid–structure interaction problems. Int J Comput Methods 8:747–757. doi:10.1142/S0219876211002794

25. Zhang ZQ, Liu GR, Khoo BC (2011) Immersed smoothed finite element method for two dimensional fluid–structure interaction problems. Int J Numer Methods Eng. doi:10.1002/nme.4299

26. Chen J-S, Wu CT, Yoon S, You Y (2001) A stabilized conforming nodal integration for Galerkin mesh-free methods. Int J Numer Methods Eng 50:435–466. doi:10.1002/nme.338

27. Liu GR (2010) A G space theory and a weakened weak (W-2) form for a unified formulation of compatible and incompatible methods: part I theory. Int J Numer Methods Eng 81:1093–1126. doi:10.1002/nme.2719

28. Liu GR (2010) A G space theory and a weakened weak (W-2) form for a unified formulation of compatible and incompatible methods: part II applications to solid mechanics problems. Int J Numer Methods Eng 81:1127–1156. doi:10.1002/nme.2720

29. Liu GR (2009) Mesh free methods: moving beyond the finite element methods, 2 edn. CRC Press, Boca Raton

30. Liu GR (2009) On G space theory. Int J Comput Methods 6:257–289. doi:10.1142/S0219876209001863

31. Liu GR, Zhang GY (2009) A normed G space and weakened weak (W2) formulation of a cell-based smoothed point interpolation method. Int J Comput Methods 6:147–179. doi:10.1142/S0219876209001796

32. Liu GR (2008) A generalized gradient smoothing technique and the smoothed bilinear form for Galerkin formulation of a wide class of computational methods. Int J Comput Methods 5:199–236. doi:10.1142/S0219876208001510

33. Liu GR, Zhang GY (2008) Edge-based smoothed point interpolation methods. Int J Comput Methods 5:621–646. doi:10.1142/S0219876208001662

34. Liu GR, Nguyen-Thoi T, Lam KY (2009) An edge-based smoothed finite element method (ES-FEM) for static, free and forced vibration analyses of solids. J Sound Vib 320:1100–1130. doi:10.1016/j.jsv.2008.08.027

35. Liu GR, Nguyen-Thoi T (2010) Smoothed finite element method. CRC Press, Boca Raton

36. Hughes TJR, Franca LP, Balestra M (1986) A new finite-element formulation for computational fluid-dynamics. 5. circumventing the Babuska-Brezzi condition—a stable Petrov-Galerkin formulation of the Stokes problem accommodating equal-order interpolations. Comput Methods Appl Mech Eng 59:85–99. doi:10.1016/0045-7825(86)90025-3

37. Tezduyar TE, Mittal S, Ray SE, Shih R (1992) Incompressible-flow computations with stabilized bilinear and linear equal-order-interpolation velocity-pressure elements. Comput Methods Appl Mech Eng 95:221–242. doi:10.1016/0045-7825(92)90141-6

38. Brooks AN, Hughes TJR (1982) Streamline upwind Petrov-Galerkin formulations for convection dominated flows with particular emphasis on the incompressible Navier-Stokes equations. Comput Methods Appl Mech Eng 32:199–259. doi:10.1016/0045-7825(82)90071-8

39. Tezduyar TE, Behr M, Liou J (1992) A new strategy for finite-element computations involving moving boundaries and interfaces-the deforming-spatial-domain space–time procedure. 1. The concept and the preliminary numerical tests. Comput Methods Appl Mech Eng 94:339–351. doi:10.1016/0045-7825(92)90059-S

40. Donea J (1984) A Taylor-Galerkin method for convective-transport problems. Int J Numer Methods Eng 20:101–119. doi:10.1002/nme.1620200108

41. Zienkiewicz OC, Taylor RL (2000) The finite element method, 5 edn. Butterworth-Heinemann, Oxford

42. Zienkiewicz OC, Nithiarasu P, Codina R, Vázquez M, Ortiz P (1999) The characteristic-based-split procedure: an efficient and accurate algorithm for fluid problems. Int J Numer Methods Fluids 31:359–392. doi:10.1002/(sici)1097-0363(19990915)

43. Belytschko T, Liu WK, Moran B (2000) Nonlinear finite elements for continua and structures. Wiley, Chichester

44. Massarotti N, Arpino F, Lewis RW, Nithiarasu P (2006) Explicit and semi-implicit CBS procedures for incompressible viscous flows. Int J Numer Methods Eng 66:1618–1640. doi:10.1002/nme.1700

45. Lai MC, Peskin CS (2000) An immersed boundary method with formal second-order accuracy and reduced numerical viscosity. J Comput Phys 160:705–719. doi:10.1006/jcph.2000.6483

46. Boffi D, Gastaldi L, Heltai L (2007) On the CFL condition for the finite element immersed boundary method. Comput Struct 85:775–783. doi:10.1016/j.compstruc.2007.01.009

47. Zhao H, Freund JB, Moser RD (2008) A fixed-mesh method for incompressible flow-structure systems with finite solid deformations. J Comput Phys 227:3114–3140. doi:10.1016/j.jcp.2007.11.019

48. Mordant N, Pinton JF (2000) Velocity measurement of a settling sphere. Eur Phys J B 18:343–352. doi:10.1007/PL00011074

49. Johnson AA, Tezduyar TE (1996) Simulation of multiple spheres falling in a liquid-filled tube. Comput Methods Appl Mech Eng 134:351–373. doi:10.1016/0045-7825(95)00988-4

50. Johnson AA, Tezduyar TE (1997) 3D simulation of fluid–particle interactions with the number of particles reaching 100. Comput Methods Appl Mech Eng 145:301–321. doi:10.1016/s0045-7825(96)01223-6

51. Johnson AA, Tezduyar TE (1999) Advanced mesh generation and update methods for 3D flow simulations. Comput Mech 23:130–143. doi:10.1007/s004660050393

52. Johnson A, Tezduyar T (2001) Methods for 3D computation of fluid–object interactions in spatially periodic flows. Comput Methods Appl Mech Eng 190:3201–3221. doi:10.1016/s0045-7825(00)00389-3

53. Turek S, Hron J (2006) Proposal for numerical benchmarking of fluid–structure interaction between an elastic object and laminar incompressible flow In: Bungartz H-J, Schäfer M (eds) Fluid–structure interaction (Lecture Notes in Computational Science and Engineering) Springer, Berlin, Heidelberg, pp. 371–385

54. Heil M, Hazel AL, Boyle J (2008) Solvers for large-displacement fluid–structure interaction problems: segregated versus monolithic approaches. Comput Mech 43:91–101. doi:10.1007/s00466-008-0270-6